Generalized Riemann Problems: From the Scalar Equation to Multidimensional Fluid Dynamics

Matania Ben-Artizi* and Joseph Falcovitz

Institute of Mathematics, the Hebrew University of Jerusalem, Jerusalem 91904, Israel
**E-mail: mbartzi@math.huji.ac.il*

The Generalized Riemann Problem (GRP) is the initial-value problem for nonlinear hyperbolic systems of (quasi) conservation laws, in one space dimension. The initial data in this case are piecewise linear, with possible jump discontinuities (of the unknowns and their slopes). The classical Riemann Problem (RP) serves as a primary "building block" in the construction of many numerical schemes (most notably the Godunov scheme). Likewise, the GRP plays a key role in the design of second-order high-resolution schemes (e.g., the MUSCL scheme). The analytic study of the GRP, both for scalar conservation laws and for systems, leads to an array of "GRP schemes" which generalize the Godunov method and at the same time are explicit, robust numerical algorithms, capable of resolving complex multidimensional fluid dynamical problems. (M. Ben-Artzi and J. Falcovitz, "Generalized Riemann Problems in Computational Fluid Dynamics", Cambridge University Press, 2003). The paper reviews the basic theory in the scalar case, with special attention to the surprising complexity of scalar 2-D "Riemann-type" problems (the Guckenheimer equation). The GRP analysis is then extended to the case of quasi 1-D compressible, inviscid, non-isentropic flow. The basic analytic facts and the resulting numerical algorithms are outlined. Special attention is devoted to the "Acoustic Approximation", which is a very simple (yet second-order) modification of the Godunov scheme. Some simulations of rather complex two-dimensional flows are presented and compared with experimental data.

Keywords: Hyperbolic conservation laws, generalized Riemann problem, second-order scheme, compressible non-isentropic quasi 1-D flow, two-dimensional interactions, acoustic approximation, Godunov and MUSCL schemes.

1. Introduction

Hyperbolic systems of conservation laws govern a large body of natural phenomena related to the time evolution of compressible, inviscid, non-isentropic gas flow. It leads to complex wave patterns resulting from multiple interactions of "elementary" waves, namely shocks, contact disconti-

nuities and rarefaction waves.

In this review we give an outline of a systematic approach to the numerical simulation of such phenomena, based on the GRP (Generalized Riemann Problem) method.

Let us first consider entropy solutions to the initial value problem for scalar conservation laws

$$\frac{\partial u}{\partial t}+\frac{\partial f(u)}{\partial x}=0, \qquad x\in\Re, \quad t\geq 0, \tag{1}$$

subject to initial data

$$u(x,t=0)=u_0(x)\in L^\infty(\Re)\cap BV(\Re), \tag{2}$$

where BV is the space of functions of bounded variation. We assume that the flux function $f:\Re\to\Re$ is C^2 and strictly convex, $f''(u)\geq\mu>0$.

As is well–known[25] the nonlinearity of flux leads to the formation of singularities of solutions $u(x,t)$ in a finite time even for very smooth initial data (2). Thus *a global solution* $u(x,t)\in L^\infty(\Re\times\Re_+)$ *must be understood in the weak (distribution) sense, namely for every test function* $\phi(x,t)\in C_0^\infty(\Re\times\overline{\Re}_+)$

$$\int_0^\infty\int_{-\infty}^\infty(u\frac{\partial\phi}{\partial t}+f(u)\frac{\partial\phi}{\partial x})dxdt+\int_{-\infty}^\infty u_0(x)\phi(x,0)dx=0. \tag{3}$$

Furthermore such weak solutions are not unique and a suitable condition is needed to select the "correct" solution. The latter is usually meant to be the one obtained by Kruzkov's vanishing viscosity approach.[18] We refer the reader to[10] for general background on various entropy conditions.

We now introduce the high-resolution second-order GRP scheme in the framework of the scalar case (1). At each time level t_n, it is assumed that the solution $u(x,t_n)$ is approximated by a piecewise linear function. More specifically, we take an equally spaced grid in $\Re$, $x_{j+\frac{1}{2}}=(j+\frac{1}{2})h$, $j\in\mathbb{Z}$, and assume that

$$v^n(x)=v_j^n+(x-x_j)s_j^n, \qquad x\in(x_{j-\frac{1}{2}},x_{j+\frac{1}{2}}). \tag{4}$$

In particular, the value v_j^n is the average of $v^n(x)$ in "cell j" $(=(x_{j-\frac{1}{2}},x_{j+\frac{1}{2}}))$ and is associated with its center $x_j=\frac{1}{2}(x_{j-\frac{1}{2}}+x_{j+\frac{1}{2}})$, and s_j^n is the slope of $v^n(x)$ in cell j.

In general terms, the idea (initiated by van–Leer[27]) is to obtain the approximation $v^{n+1}(x)$ at time $t_{n+1}=t_n+k$ by solving Eq. (1) with initial data $U(x,t_n)=v^n(x)$. Let $U(x,t)$ be the solution. The function $v^{n+1}(x)$ is then evaluated as a suitable approximation to the exact solution $U(x,t_{n+1})$. In the piecewise constant case ($s_j^n=0$ for all j), this leads to the Godunov

scheme.[11] The values v_j^{n+1} are the exact averages of the solution $U(x, t_{n+1})$. This exact evaluation is of course due to the fact that in this case the solution $U(x,t)$ consists of an array of solutions to Riemann problems, and the resulting fluxes $f(U(x_{j+\frac{1}{2}}, t))$, $(t_n \le t \le t_{n+1})$, are constant in time.

For our second order case ($s_j^n \neq 0$ in general) a similar study for analytic evaluation of the fluxes $f(U(x_{j+\frac{1}{2}}, t))$ leads to the generalized Riemann problem (**GRP**). For the given initial distribution (4), one cannot expect to have a full knowledge of the fluxes $f(U(x_{j+\frac{1}{2}}, t))$, and they are replaced by some linear approximations in t. One particular way of doing it is the GRP method,[1] which is the focus of our discussion here, and which we shall recall in detail in the next section, in the context of 1-D scalar equations.

In Sections 3–4, we turn to the two-dimensional scalar equation and discuss the important case of "Riemann type" problems. They allow for fully analytic solutions which nevertheless display an impressive variety of complex wave structures, resulting from multidimensional interactions of elementary waves. In particular, we review in Section 5 the analytical and numerical treatment of the Guckenheimer equation. Section 6 serves as a reminder of the system of quasi 1-D compressible flow in ducts of variable cross-section. We outline the basic properties of the GRP approach to this system in Section 7, leading to the GRP numerical scheme (Section 8). Section 9 is devoted to some fluid dynamical examples, including comparison with experimental data.

2. GRP Scheme – Basic Properties

We let $U(x,t)$ be the exact solution to (1),(4), $t \ge t_n$, with $U(x, t_n) = v^n(x)$.

With notations as introduced above, the approximate averages v_j^{n+1} are determined by

$$v_j^{n+1} = v_j^n - \lambda(f_{j+\frac{1}{2}}^{n+\frac{1}{2}} - f_{j-\frac{1}{2}}^{n+\frac{1}{2}}), \tag{5}$$

where $\lambda = \frac{k}{h}$ and the numerical flux $f_{j+\frac{1}{2}}^{n+\frac{1}{2}}$ should approximate the time average of $f(U(x_{j+\frac{1}{2}}, t))$, $t_n \le t \le t_{n+1} = t_n + k$. Recall that the conservation law (1) is now solved subject to the initial condition $v^n(x)$ as in (4), where the cells are of uniform size $h = x_{j+\frac{1}{2}} - x_{j-\frac{1}{2}}$.

In the first step, we evaluate $v_{j+\frac{1}{2}}^n$ by

$$v_{j+\frac{1}{2}}^n = R(0; v_{j+\frac{1}{2},\mp}^n), \tag{6}$$

where $R(\frac{x}{t}; w_\mp)$ is the (self-similar) solution to the Riemann problem for (1), having initial data $w_\mp$ for $\mp x > 0$. The limiting values $v_{j+\frac{1}{2},\mp}^n$ appearing

in Eq. (6) are defined by

$$v^n_{j+\frac{1}{2},\mp} = \lim_{x \to x_{j+\frac{1}{2}}\mp} v^n(x). \tag{7}$$

Thus, the value $v^n_{j+\frac{1}{2}}$ is the "instantaneous" value obtained by solving the Riemann problem with the limiting values of $v^n(x)$ at the cell boundary $x_{j+\frac{1}{2}}$. In our case (f strictly convex), the Riemann solution is determined simply as follows.

(i) $v^n_{j+\frac{1}{2}} = v_{\min}$, the minimum point of $f(v)$, if $v^n_{j+\frac{1}{2},-} \le v_{\min} \le v^n_{j+\frac{1}{2},+}$. In this case we say that $x_{j+\frac{1}{2}}$ is a sonic point. Otherwise,
(ii) $v^n_{j+\frac{1}{2}} = w$ such that $f(w) = \min\{f(v); v \in [v^n_{j+\frac{1}{2},-}, v^n_{j+\frac{1}{2},+}]\}$ if $v^n_{j+\frac{1}{2},-} \le v^n_{j+\frac{1}{2},+}$ (rarefaction), or,
(iii) $v^n_{j+\frac{1}{2}} = w$ such that $f(w) = \max\{f(v); v \in [v^n_{j+\frac{1}{2},+}, v^n_{j+\frac{1}{2},-}]\}$ if $v^n_{j+\frac{1}{2},+} \le v^n_{j+\frac{1}{2},-}$ (shock).

We note that the wave moves to the right (resp. the left) if $f'(v^n_{j+\frac{1}{2}}) > 0$ (resp. $f'(v^n_{j+\frac{1}{2}}) < 0$). *The key ingredient in the GRP method is the assumption that both $U(x_{j+\frac{1}{2}}, t)$ and $f(U(x_{j+\frac{1}{2}}, t))$ are approximated linearly (in $t \in [t_n, t_{n+1}]$).* We obtain therefore the linear expressions,

$$\begin{aligned} &(i)\ \ \tilde{u}(x_{j+\frac{1}{2}}, t) = v^n_{j+\frac{1}{2}} + \left(\tfrac{\partial U}{\partial t}\right)^n_{j+\frac{1}{2}} (t - t_n), \\ &(ii)\ \tilde{f}(\tilde{u}(x_{j+\frac{1}{2}}, t)) = f(v^n_{j+\frac{1}{2}}) + f'(v^n_{j+\frac{1}{2}}) \left(\tfrac{\partial U}{\partial t}\right)^n_{j+\frac{1}{2}} (t - t_n). \end{aligned} \tag{8}$$

The exact instantaneous value of $\left(\frac{\partial U}{\partial t}\right)^n_{j+\frac{1}{2}}$ at the cell boundary is obtained from (1),

$$\left(\frac{\partial U}{\partial t}\right)^n_{j+\frac{1}{2}} = \begin{cases} -f'(v^n_{j+\frac{1}{2}}) s^n_j, & \text{if the wave moves to the right,} \\ -f'(v^n_{j+\frac{1}{2}}) s^n_{j+1}, & \text{if the wave moves to the left,} \\ 0, & \text{if } x_{j+\frac{1}{2}} \text{ is a sonic point.} \end{cases} \tag{9}$$

Incorporating these formulas in (5), we DEFINE the GRP fluxes:

$$f^{n+\frac{1}{2}}_{j+\frac{1}{2}} = \tilde{f}(\tilde{u}(x_{j+\frac{1}{2}}, t_n + \frac{k}{2})), \qquad -\infty < j < \infty. \tag{10}$$

and then v^{n+1}_j is determined by (5). The new slopes s^{n+1}_j are calculated in two steps.

Step 1. Determine $v_{j+\frac{1}{2}}^{n+1} = \tilde{u}(x_{j+\frac{1}{2}}, t_{n+1})$ by Eq. (8)(i) and then set

$$\tilde{s}_j^{n+1} = \frac{1}{h}(v_{j+\frac{1}{2}}^{n+1} - v_{j-\frac{1}{2}}^{n+1}). \tag{11}$$

Step 2. ("Limiter Algorithm"). Set the final value for some $\theta \in (0, 2]$,

$$s_j^{n+1} = \frac{1}{h}\text{minmod}((2-\theta)(v_{j+1}^{n+1}-v_j^{n+1}),\, h\tilde{s}_j^{n+1},\, (2-\theta)(v_j^{n+1}-v_{j-1}^{n+1})), \tag{12}$$

where the minmod function is defined by,

$$\text{minmod}(a,b,c) = \begin{cases} \sigma \min(|a|,|b|,|c|), & \text{if } \sigma = \text{sign}(a) = \text{sign}(b) = \text{sign}(c), \\ 0, & \text{otherwise,} \end{cases}$$

Remark 2.1. Geometrically speaking, our limiter satisfies the "minimal" change needed in implementing the following "5–point rule": If $\{v_{j-1}^{n+1}, v_j^{n+1}, v_{j+1}^{n+1}\}$ form a monotone increasing sequence, then so are the five values
$\{v_{j-1}^{n+1}, v_j^{n+1} - \frac{h}{2}s_j^{n+1}, v_j^{n+1}, v_j^{n+1} + \frac{h}{2}s_j^{n+1}, v_{j+1}^{n+1}\}$, see Fig. 2. However $\theta < 1$ leads to "sawtooth", i.e., the profile of $v^{n+1}(x)$ for $x \in [x_j, x_{j+1}]$ is not necessarily monotone.

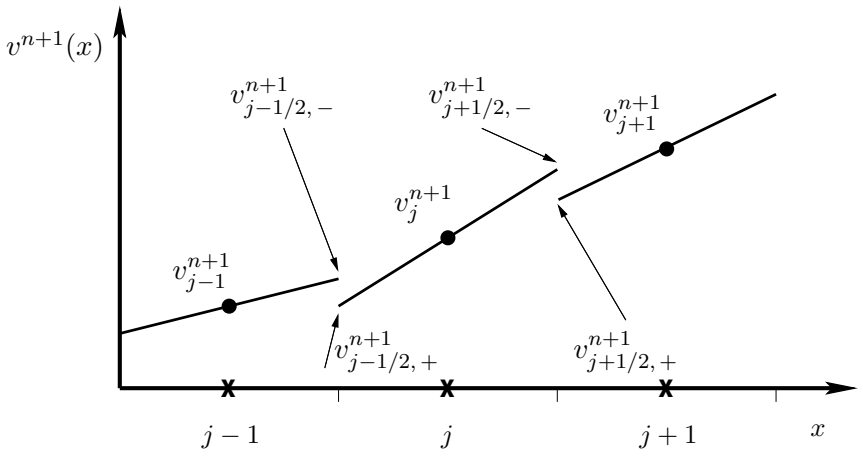

Fig. 1. The notations $v_{j\mp\frac{1}{2},\pm}^{n+1}$ are for $v_j^{n+1} \mp \frac{h}{2}s_j^{n+1}$ respectively.

3. Self-Similar Solutions in 2-D

Turning to a two-dimensional setting, we now consider the initial value problem (IVP) for a scalar equation,

$$u_t + f(u)_x + g(u)_y = 0, \tag{13}$$

$$u(x, y, 0) = \phi(x, y), \quad (x, y) \in \Re^2, \tag{14}$$

where $u(x, y, t)$ is a real (scalar) function and $f(u)$, $g(u)$ are real smooth flux functions.

A "Riemann type" problem for (13) is the IVP where $\phi(x, y)$ is finitely valued and homogeneous of order zero,

$$\phi(x, y) = u_0(\theta), \quad \theta = \arg(x, y)(= \arctan \frac{y}{x}), \tag{15}$$

and $u_0(\theta)$ is piecewise constant in $[0, 2\pi]$ with finitely many jumps.

Recall (see[13]) and the original papers[18,28]) that, for any initial function $\phi \in L^\infty(\Re^2)$, there exists a unique (weak) solution $u(x, y, t)$ to Eqs. (13)–(14). The entropy condition (which contains already the fact that u is indeed a weak solution) can be described as follows.

Let $U(s)$ be a real convex function and $F(s)$ and $G(s)$ functions such that

$$F'(s) = U'(s)f'(s), \quad G'(s) = U'(s)g'(s). \tag{16}$$

Then, in the sense of distributions,

$$U(u)_t + F(u)_x + G(u)_y \leq 0. \tag{17}$$

The initial value (14) is attained in the sense that

$$u(x, y, t) \to \phi(x, y) \quad \text{in } L^1_{loc}(\Re^2), \quad \text{as } t \to 0+. \tag{18}$$

When the initial data is given by (15), the uniqueness implies that the solution is "self-similar", namely,

$$u(x, y, t) = u(x/t, y/t, 1), \quad t > 0. \tag{19}$$

In what follows we shall use the similarity coordinates

$$\xi = \frac{x}{t}, \quad \eta = \frac{y}{t}, \tag{20}$$

and set $v(\xi, \eta) = u(\xi, \eta, 1)$.

The solutions to the Riemann–type problem Eqs. (13)–(15) display an extremely rich variety of wave patterns, some of which are far from being "evident". We refer to[12,20,29,30] for a thorough presentation. Our intention

in this review is to show that this variety can serve as a basis for the investigation of "fine points and subtleties" pertinent to high resolution schemes. Unlike the "one–dimensional test cases" (most of which have been carried out only for the Burgers equation), the truly two–dimensional wave structures, combined with the inherent "spatial splitting" of the numerical schemes, poses a considerable challenge. We remark that the description of geometric shapes in Cartesian grids presents already a nontrivial difficulty for the schemes (see[3]).

4. The Analysis of 2-D Riemann–Type Solutions

We recall here the basic facts concerning solutions to Eqs. (13)–(15). Using the similarity notation (19)–(20), we refer to the solution as $v(\xi,\eta)$. Note that the initial condition (15) now becomes

$$u_0(\theta) = \lim_{r\to\infty} v(r\cos\theta, r\sin\theta), \quad 0 \le \theta \le 2\pi. \tag{21}$$

In general terms, the IVP can be cast in terms of an equation for v (in the (ξ,η) plane) with a boundary condition (21) imposed at the "circle at infinity". In fact, due to finite propagation speed, the solution consists of separate 1–D waves i (emanating from rays in direction of the jumps of $u_0(\theta)$). These waves interact in a disk centered at the origin, and the difficulty lies in the need to account for the interactions, subject to the entropy conditions.

In regions of smooth flow (i.e., where $v(\xi,\eta) \in C^1$), we have from (13),

$$(-\xi + f'(v))v_\xi + (-\eta + g'(v))v_\eta = 0, \tag{22}$$

which is a quasilinear equation. Its characteristic curves carry constant values of v, and are therefore straight lines (terminating at singularities). Let L_C be the line carrying the value $v = C$. By (22) it is an integral line for the field $\Phi_C(\xi,\eta) = (-\xi + f'(C), -\eta + g'(C))$, hence lies on a ray emanating from the critical point $z_C := (f'(C), g'(C))$. We orient it, by convention, in the direction of z_C.

Remark 4.1. Note that by (13), the characteristic lines L_C are just the traces of the bicharacteristic lines for (13) on the (x,y) plane, now identified as the (ξ,η) plane. The chosen orientation for L_C (toward z_C) corresponds to orienting the bicharacteristic line in the direction $t \to +\infty$ (so that $(\xi,\eta) = (\frac{x}{t}, \frac{y}{t})$ approaches z_C).

Definition 4.1. The "critical set" $\Gamma(v)$ for Eq. (22) is the set of all possible points z_C, i.e.,

$$\Gamma(v) = \{(f'(C), g'(C)), C = v(z_C), \text{ for some } z_C \in \Re^2\}. \tag{23}$$

We now turn to conditions imposed on jump discontinuities of solutions to (22). Using the standard procedure for the definition of weak solutions, we obtain the Rankine–Hugoniot jump relations.

Claim 4.1. *Let $\eta = \eta(\xi)$ be the (C^1) trajectory of a jump discontinuity. Then the slope $\sigma = \eta'(\xi)$ satisfies the R–H condition*

$$\sigma = \frac{\eta - g'_{+,-}}{\xi - f'_{+,-}}, \tag{24}$$

where $h'_{+,-} = \frac{h(v_+)-h(v_-)}{v_+-v_-}$ and $v_\pm$ are the limiting values of the solution v at the jump.

proof Note that by the standard procedure (see[13]) applied to (22) in the form

$$(-\xi v + f(v))_\xi + (-\eta v + g(v))_\eta + 2v = 0, \tag{25}$$

we get

$$\sigma = \frac{-\eta(v_+ - v_-) + g(v_+) - g(v_-)}{-\xi(v_+ - v_-) + f(v_+) - f(v_-)},$$

which reduces to (24). □

Remark 4.2. As in the case of Remark 4.1, the R–H condition (24) can be derived by applying the notion of a weak solution directly to Eq. (13). In this case, a surface of discontinuity in the (x, y, t) variables is expressed in a self-similar form $y = t\eta(\frac{x}{t})$, and the R–H condition is applied to the normal direction $(\sigma, -1, \eta - \xi\sigma)$, where $\sigma = \eta'(\xi)$ (and $(\xi, \eta) = (\frac{x}{t}, \frac{y}{t})$). In particular, the "effective" flux function in this direction (see[13]) is

$$H_\sigma(v) = \sigma f(v) - g(v). \tag{26}$$

The entropy (admissibility) condition on jump discontinuities is most easily obtained by resorting to the (x, y, t) setting and the "directional" flux H_σ, as in (26). Using the convention $v_- < v_+$, we get

$$\frac{H_\sigma(k) - H_\sigma(v_-)}{k - v_-} \geq \frac{H_\sigma(v_+) - H_\sigma(v_-)}{v_+ - v_-}, \quad k \in [v_-, v_+] \tag{27}$$

as a necessary and sufficient condition for a jump (v_-, v_+) whose slope is $\sigma = \eta'(\xi)$.

In analogy with $\Gamma(v)$ (see (23)), we define the set (for a given solution v and a fixed state $\bar{v}$),

$$\Gamma_s(v;\bar{v}) = \{(f'_{+,-}, g'_{+,-}), v_- = \bar{v}, v_+ = v(\xi_+, \eta_+) \text{ for some } (\xi_+, \eta_+) \in \Re^2\}. \tag{28}$$

In view of (24), the set $\Gamma_s(v;\bar{v})$ has the following geometric interpretation. If l is a tangent line to a smooth discontinuity curve, and v takes on the value $\bar{v}$ at the tangency point (on either side) then l intersects $\Gamma_s(v;\bar{v})$.

The entropy condition (27) implies, as is well–known, that all bicharacteristic lines (in (x,y,t)) "impinge" on the shock surface, as $t \to +\infty$ (or are tangent to it). In view of Remark 4.1 and our convention for the orientation of characteristic curve in the (ξ,η) plane, we obtain the following corollary.

Corollary 4.1. *If $\eta = \eta(\xi)$ is the trajectory of an admissible shock, then the characteristic lines on its two sides run "into it" (with the given orientation) or are tangent to it (so that the shock becomes sonic on that side).*

The structure of a centered rarefaction wave (CRW) in the (ξ,η) plane is derived from the discussion of characteristic lines and their directions. For clarity we state it in the following claim.

Claim 4.2. *A CRW centered at (ξ_0,η_0) is given by the sector*

$$\alpha \le \frac{\eta - \eta_0}{\xi - \xi_0} \le \beta,$$

where, for any direction $r \in [\alpha,\beta]$, $v = C_r$ such that

$$r = \frac{g'(C_r) - \eta_0}{f'(C_r) - \xi_0}. \tag{29}$$

Remark 4.3. Observe that this CRW corresponds to a rather complex structure in the original (x,y,t) setting; the vertex (ξ_0,η_0) represents the line $x = \xi_0 t$, $y = \eta_0 t$. At any time t there is a (rarefaction) fan of rays emanating from (x,y,t) and carrying constant values of u. The whole structure moves in a self-similar fashion as t increases. The rays then become planes (carrying constant values of u) whose traces on the (ξ,η) plane satisfy (29).

We can summarize the procedure for the solution of the Riemann–type problem Eqs. (13)–(15) as follows.

(a) The problem is restated as Eq. (22) in the (ξ, η) plane, where the function $v(\xi, \eta)$ satisfies the boundary condition (21).
(b) Outside of a sufficiently large disk (in (ξ, η)) we determine the 1–D waves issuing at the jump discontinuities of $u_0(\theta)$ in the (x, y, t) setting, and determine $v(\xi, \eta) = u(\xi, \eta, 1)$.
(c) The resulting waves are extended into the disk, where they interact and produce additional waves (CRW or shocks), subject to the conditions (27) (shocks) and (29) (CRW).

As we shall see in the following section, this last step can be quite involved, producing surprising structures. For general treatments, we refer to.[12,20,30]

5. The 2-D Guckenheimer Equation

A very instructive example is provided by the Riemann-type problem for the two-dimensional scalar conservation law, due to Guckenheimer,[12]

$$\frac{\partial}{\partial t}u + \frac{\partial}{\partial x}(u^2/2) + \frac{\partial}{\partial y}(u^3/3) = 0, \tag{30}$$

$$u(x, y, 0) = u_0(\theta) = \begin{cases} 0 & \text{in sector} \quad 0 < \theta < \frac{3\pi}{4}, \\ 1 & \text{in sector} \quad \frac{3\pi}{4} < \theta < \frac{3\pi}{2}, \\ -1 & \text{in sector} \quad \frac{3\pi}{2} < \theta < 2\pi, \end{cases} \tag{31}$$

where $\theta = \arctan(\frac{y}{x})$ (see also Fig. 2(a)). The flux functions here are not identical. Moreover, the function $g(u)=u^3/3$ is nonconvex, and as we shall see below, this produces a solution with a "sonic shock". Note that in this case the solution to the Riemann problem (and likewise to the generalized Riemann problem) needs to be modified, taking into account the nonconvexity of $g(u)$. In the present case this modification is rather simple (see [9, Section 2.6 and Remark 2.2 in Section 3.2]).

Consider the (self-similar) exact solution (see[4,12,20,30]) of (30)–(31), shown in Fig. 2(b). Referring to this figure, we notice that outside of a large disk, the solution consists of the following three shocks:

(a) A shock emanating from the line $y = 0$ $(x > 0)$, moving at speed $1/3$ in the positive y direction (note that $g(u) = u^3/3$ is concave on $[-1, 0]$).
(b) A standing shock along $x = 0$ $(y < 0)$.
(c) A shock emanating from the line $x + y = 0$. The self-similar analysis (see[4,12]) shows that at $t > 0$ this line is given by $x + y = (5/6)t$.

The interaction of these three shocks in a disk around $(0,0)$ gives rise to a very complex wave structure. At time t=1 it can be described as follows (see Fig. 2(b)). The shock **(b)** extends to a segment of the positive y-axis $0 \le y \le b,\ b$=0.2823057. At the point $(0,b)$ it bifurcates into a CRW whose tail characteristic is a sonic shock, across which the solution $u(x,y,1)$ jumps from -1 to the value $\tilde{v} = 0.6087418$. Then u increases across the rarefaction from $\tilde{v}$ to 1, and it is constant along each (straight) characteristic line. The rarefaction wave modifies shock **(c)** in a fashion similar to that of the curved shock in the previous example of the Burgers equation (Case (D)). Note that the head characteristic of the CRW carries the value u=1. It intersects the shock **(c)** at the point (x_0, y_0) given by

$$x_0 = \frac{\frac{5}{6} - b}{2 - b}, \qquad y_0 = \frac{\frac{5}{6} + \frac{b}{6}}{2 - b}.$$

The tail characteristic (sonic shock) intersects the shock **(a)** at the point $(\tilde{\xi}, \frac{1}{3})$, where $\tilde{\xi} = 0.3519610$. The result of the interaction between the CRW and the shock **(c)** leads, as noted above, to a "bending" of the latter, forming a shock branch y=$y(x)$ connecting (x_0, y_0) to $(\tilde{\xi}, \frac{1}{3})$. It can be determined by solving an ordinary differential equation ([4]).

Thus, we obtain a wave pattern that includes a shock wave bifurcating into a CRW and a sonic shock which serves as a tail characteristic of the CRW. It intersects with the other two shocks at the triple point $(\tilde{\xi}, \frac{1}{3})$. This wave pattern provides for a good test of finite-difference schemes.

Two numerical tests were performed, one using the Godunov scheme and the other with the GRP scheme. The 2-D algorithm is obtained from the 1-D scheme by using the Strang "Splitting Method" (see [2, Chapter 7] and[26]) which ensures the second-order accuracy of the GRP scheme.

The computation domain was the square $[-1 \le x \le 1,\ -1 \le y \le 1]$ which was divided into 320×320 square cells. The time step was Δt=0.003125 (i.e., μ_{CFL}=0.5 since $max|u|$=1 and $f'(u)$=u, $g'(u)$=u^2), and the computation was performed to final time t=1. The boundary conditions were specified by calculating the exact solution on the outer segments of boundary cells. This is possible as long as the domain boundary is intersected only by the three shocks **(a), (b), (c)**, which according to Fig. 2(b) is still true at t=1.

The results are shown in the sub-domain $[-0.05 \le x \le 0.60,\ 0 \le y \le 0.65]$ (see Fig. 3(a) for the Godunov scheme, and Fig. 3(b) for the GRP scheme). Recall that inside the rarefaction fan u is constant along the (straight) characteristic lines, so that numerical U-level curves approximate the fan structure. The U-level sequence (32) given below is designed to

show the shock fronts and the rarefaction fan. The five levels $L = 9, ..., 13$ correspond to the tail, head, and three inner characteristic lines of the rarefaction fan (as shown in Fig. 2(b)).

$$U_{_L} = \begin{cases} -1 + 0.2\, L & \dots \quad L = 0, 1, ..., 8 \\ 0.60874,\ 0.68295,\ 0.76366,\ 0.86089,\ 1, & \dots \quad L = 9, ..., 13. \end{cases} \tag{32}$$

In order to enable interpolation at the lowest and highest U-levels, they were slightly shifted to -0.990 and 0.997, respectively. For comparison of the exact and numerical solutions, we represent the exact solution (Fig. 2(b)) by discrete "marker points" situated on shock fronts, as shown in Fig. 5. Additional marker points are located at points (x, y) inside the rarefaction fan, where the exact solution takes on the same values $U_{_L}$, $L = 9, ..., 13$ as given by (32).

Our primary observation with respect to the numerical solution is that both finite-difference schemes, applied according to the operator splitting produce a correct approximation to this complex 2-D wave-interaction pattern (Fig. 5). The GRP solution agrees quite well with the exact one, while the Godunov solution shows a nearly equal agreement for the shock fronts, but a lesser agreement in the rarefaction fan. In this centered fan, the characteristic line that coincides with the sonic shock front corresponds to a constant value of $u{=}\tilde{v}$, and it is one of the U-level lines plotted ($L{=}9$). In the GRP solution this line is seen very near the sonic shock front (Fig. 3(b)), while in the Godunov case its stand-off distance is perceptibly higher (Fig. 3(a)). The captured sonic shock is represented by the cluster of level lines $L = 0, ..., 9$ (since the jump across this shock is from $u{=}U_0$ to $u{=}U_9$). At the other end of the rarefaction fan, the head characteristic line is plotted with $U_{13}{=}0.997$ (close to the exact value of $U_{13}{=}1$, for a clear U-level interpolation). In the Godunov solution this line extends well beyond the exact solution, while in the GRP solution it agrees well with the exact marker points. The rarefaction fan is the only region of the solution where $u(x, y, 1)$ varies smoothly with a non-zero gradient. Hence, these observations indicate that in such regions the (second-order accurate) GRP scheme produces considerably smaller errors than the (first-order accurate) Godunov scheme. In what concerns the bifurcation point $(0, b)$ and the triple point $(\tilde{\xi}, \frac{1}{3})$, resulting from the two-dimensional setting, we observe that they are well replicated by both schemes.

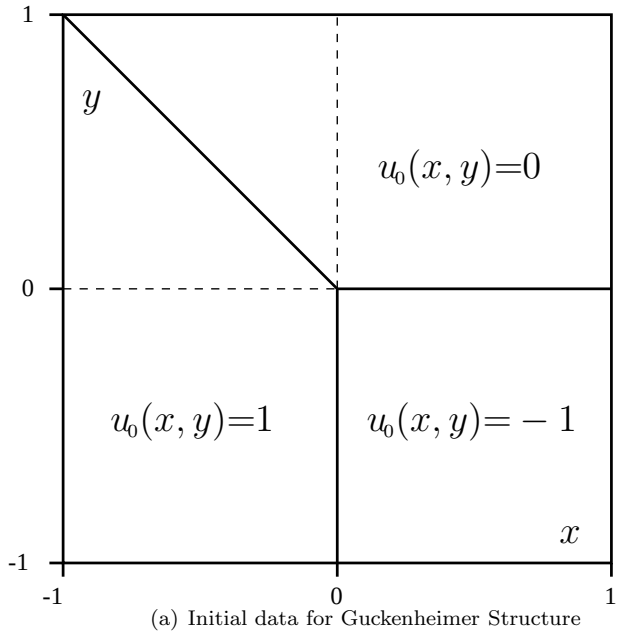

(a) Initial data for Guckenheimer Structure

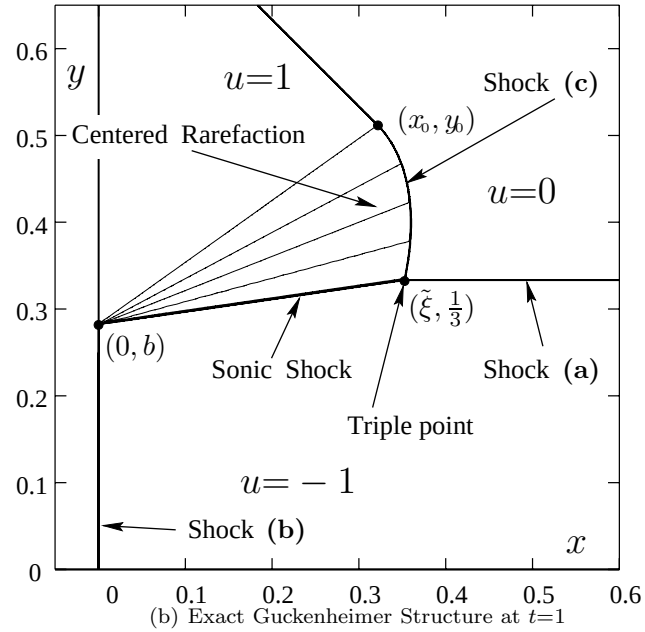

(b) Exact Guckenheimer Structure at t=1

Fig. 2. The Guckenheimer Structure for $u_t + (u^2/2)_x + (u^3/3)_y = 0$.

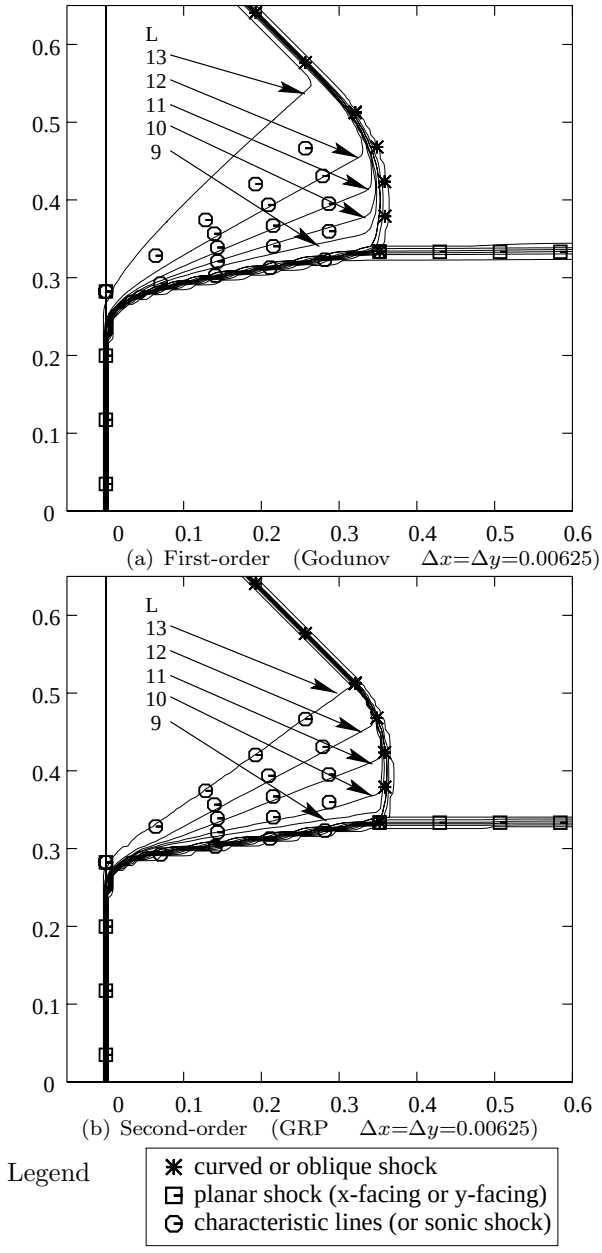

Fig. 3. U-level curves for Guckenheimer equation at t=1
$u_t + (u^2/2)_x + (u^3/3)_y = 0$. Initial data in Fig. 2(a).

6. Euler Equations of Quasi 1-D Compressible Inviscid Flow

We consider here the time-dependent flow of a compressible inviscid fluid moving through a duct of variable cross-section. The flow is assumed to be Quasi-One-Dimensional, (Quasi 1-D) namely, at any given time t the flow is uniform over every cross-section of the duct (but, of course, may vary from one cross-section to another). Thus, for a duct as depicted in Fig. 6, we let r be a spatial coordinate along the "main axis". Our hypothesis is

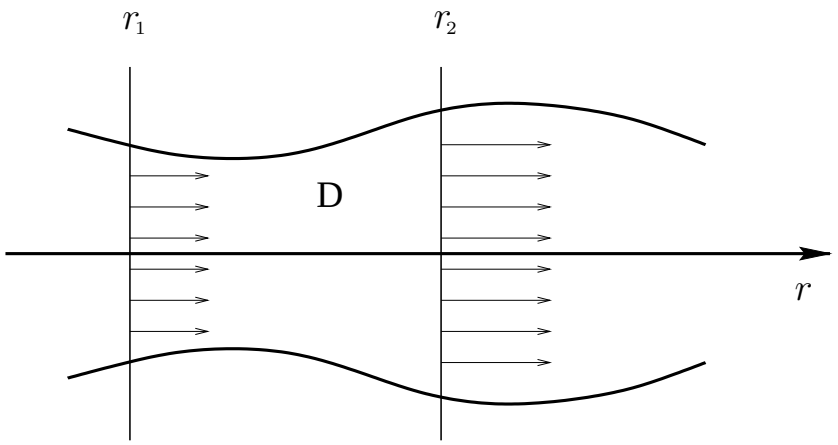

Fig. 4. Quasi 1-D flow in a duct.

then that all flow quantities (like density, pressure, velocity,...) depend only on (r, t).

Certainly, in many cases this is just a simplified model approximating a more realistic two (or three) dimensional flow, based on a physical assumption that the flow varies primarily along the duct axis. However, there are three cases of substantial physical significance, in which the model is exact.

A) Planar Flow, sometimes referred to as "one-dimensional" flow. Here the whole flow is aligned with one direction, say the x-axis. All flow quantities depend only on x (which is now the "r coordinate"), in addition to the time t. The velocity vector has only an x component $u(x, t)$.

B) Cylindrical Flow. In this case the flow is symmetric about a fixed axis, say the z-axis. The coordinate r is now $r = (x^2 + y^2)^{1/2}$ and all flow quantities are functions of (r, t). The velocity $\mathbf{v}(x, y, z, t)$ satisfies

$\mathbf{v}(x,y,z,t) = r^{-1}u(r,t)(x\mathbf{i}+y\mathbf{j})$ ($\mathbf{i},\mathbf{j},\mathbf{k}$ are the unit vectors along the x,y,z axes, respectively). Observe that the duct can now be taken as a sector $\lambda_1 x < y < \lambda_2 x, \quad 0 \le \lambda_1 < \lambda_2$, $x \ge 0$.

C) Spherical Flow. In this case the flow is symmetric about a fixed center O, the origin. The coordinate r is now the distance $(x^2+y^2+z^2)^{1/2}$ and the velocity is radial, namely $\mathbf{v}(x,y,z,t) = r^{-1}u(r,t)(x\mathbf{i}+y\mathbf{j}+z\mathbf{k})$.

The Flow Equations

We now turn to the equations governing our quasi 1-D flow. They express the three basic physical laws governing the flow: Conservation of mass, conservation of momentum (or, alternatively, Newton's second law) and conservation of energy. These laws are most easily derived by a "control volume" (or "integral") approach: One considers a fixed mass of fluid and applies the above laws to it. As is usually the case, we assume that there are no external forces (such as gravity or electromagnetic force), so that the only existing force is due to the hydrodynamic pressure. We shall give here a brief outline of the derivation, and refer the reader to fluid dynamics books, such as[5,6] or,[19] for a detailed derivation of the equations.

Let $A(r)$ be the cross-sectional area of the duct at r. Clearly, $A(r) \equiv 1$ for planar flow, $A(r) = r$ for cylindrical flow, and $A(r) = r^2$ for spherical flow. There are three unknown functions. The velocity $u(r,t)$, which is the (scalar) component along the r-axis, the density (mass per unit volume) $\rho(r,t)$, and the total specific energy (per unit mass) $E(r,t)$. The energy E consists of the kinetic energy (per unit mass) $\frac{1}{2}u^2$ and the internal (thermodynamic) energy e, so that $E = \frac{1}{2}u^2 + e$. A basic thermodynamic postulate in the derivation of the equations is that the hydrodynamic pressure p is a function $p = p(e,\rho)$. We refer to this function as the equation-of-state of the fluid. The resultant force on a given volume D of the fluid is then $-\int\limits_{\partial D} p\mathbf{n}\, d\sigma = -\int\limits_{D} \boldsymbol{\nabla} p\, d\tau$, where ∂D is the boundary of D, $d\sigma$ the surface element, $d\tau$ the volume element, and $\mathbf{n}$ the outward (unit) normal to ∂D. The equality above follows by Stokes' theorem. Similarly, the work done by the pressure on the fluid (per unit time) is $-\int\limits_{D} \boldsymbol{\nabla}\cdot(p\mathbf{v})\, d\tau$, where $\mathbf{v}$ is the velocity vector. Note also that the outflux (per unit time) across ∂D, for any quantity ψ (in our case $\psi = \rho$ or $\psi = \rho E$) is $\int\limits_{\partial D} \psi(\mathbf{v}\cdot\mathbf{n})\, d\sigma$. We can now take D as the segment $r_1 \le r \le r_2$ of the duct (see Fig. 6). Incorporating the above considerations into the balance equations for mass, momentum and energy, and letting $r_2 - r_1$ go to zero, we obtain the conservation equations

in differential form as follows.

$$\begin{aligned}
&\text{(i)} && \tfrac{\partial}{\partial t}\rho + A^{-1}\tfrac{\partial}{\partial r}[A\rho u] && = 0 \quad \text{(conservation of mass)},\\
&\text{(ii)} && \tfrac{\partial}{\partial t}(\rho u) + A^{-1}\tfrac{\partial}{\partial r}[A\rho u^2] + \tfrac{\partial p}{\partial r} && = 0 \quad \text{(conservation of momentum)},\\
&\text{(iii)} && \tfrac{\partial}{\partial t}(\rho E) + A^{-1}\tfrac{\partial}{\partial r}[A(\rho E + p)u] = 0 && \quad \text{(conservation of energy)},
\end{aligned} \tag{33}$$

where the equation-of-state $p = p(e, \rho)$ is given.

We can write the system (33) as

$$\frac{\partial}{\partial t}\mathbf{U} + A^{-1}\frac{\partial}{\partial r}\big[A\mathbf{F}(\mathbf{U})\big] + \frac{\partial}{\partial r}\mathbf{G}(\mathbf{U}) = 0\,, \tag{34}$$

$$\mathbf{U} = \begin{bmatrix} \rho \\ \rho u \\ \rho E \end{bmatrix}, \qquad \mathbf{F}(\mathbf{U}) = \begin{bmatrix} \rho u \\ \rho u^2 \\ (\rho E + p)u \end{bmatrix}, \qquad \mathbf{G}(\mathbf{U}) = \begin{bmatrix} 0 \\ p \\ 0 \end{bmatrix}.$$

The presence of the function $A(r)$ means that the system (34) cannot be cast in the (strict) form of "Conservation Laws" (i.e., $A^{-1}(A\mathbf{F}(\mathbf{U}))_r$ cannot, in general, be written as $(\tilde{\mathbf{F}}(\mathbf{U}))_r$ for some $\tilde{\mathbf{F}}$). However, this is possible in the planar case $A(r) \equiv 1$. As in the case of a scalar equation, the Riemann problem plays a key role in the design of a numerical scheme for (34). It is the initial value problem for the equation, subject to the initial data

$$\mathbf{U}(r, 0) = \begin{cases} \mathbf{U}_L\,, & r < 0\,, \\ \mathbf{U}_R\,, & r > 0\,. \end{cases} \tag{35}$$

In the planar case, one obtains the well-known self-similar solution, which consists of three waves. The middle one is a contact discontinuity while each one of the other two is either a shock or a rarefaction wave.[6] The full construction of the solution is reduced to solving a pair of algebraic equations that express the continuity of the pressure and velocity across the contact discontinuity. In the general case considered here it has been observed that (34) is not in "conservation form", hence the solution to the Riemann problem is no longer self-similar, and can no longer be obtained solely by algebraic means. However, due to the "finite propagation speed" property of the equation this solution retains some features of the self-similar one. More specifically, near $r = 0$ the wave pattern (in particular the nature and strength of the waves at the singularity) is identical to that of the "associated" solution obtained by "freezing" the cross-section area $A(r)$ at the constant value $A(0)$. Note, however, that the (r, t) trajectories of

the waves emanating from the singularity are curvilinear, and their speeds vary in time, as a result of the non-uniformity of the cross-section $A(r)$. The reader is referred to[2] for more details. We also point out that Appendix C in[2] gives an efficient algorithm for the solution of the Riemann problem in the special case (but very important in applications and numerical tests) of a γ-law gas. In what follows, we introduce the "Generalized Riemann Problem" associated with (34).

7. The GRP for Quasi 1-D Compressible Inviscid Flow

In Section 6 we considered the Euler equations (34) governing the quasi 1-D flow in a duct of variable cross-section. We emphasized in particular the role of the Riemann problem ("shock tube problem"), namely the IVP subject to initial data (35). As we have already noted, the solution to the Riemann problem is a basic ingredient in the numerical resolution of the flow. It was observed that in the planar case of uniform cross-sectional area this solution is "self-similar" and is readily obtained by solving a pair of algebraic equations. However, as is well known (even in the scalar case), such a scheme ("Godunov's scheme") yields poor results in the resolution of singularities. It has been widely demonstrated that the resolution is greatly improved when switching to piecewise-linear data, thus leading to the Generalized Riemann Problem. Turning back to the quasi 1-D system (34), we noted that it is not in strict conservation form. In particular, one cannot expect here a self-similar solution to the Riemann problem, implying that it cannot be reduced to an algebraic problem, as in the planar case. Thus, in dealing with the general case, we have to resort to further analysis of the problem, even in the case of initial data as in (35) (see also[8] in this case). Replacing the piecewise constant by piecewise linear initial data brings about a dramatic improvement in the numerical results. This was first established for the fluid-dynamical case in the pioneering work of van Leer (see[27]). We shall therefore concentrate in this section on the IVP for the system (34), with initial data which are linear on the two sides of the singularity, across which both the functions and their slopes may experience a jump. The term "Generalized Riemann Problem" (GRP) has been attached to this problem (see[1]) and we shall employ it henceforth.

Structure of the Solution to the GRP

Let $\mathbf{U}(r,t)$ be the solution to the GRP, namely the IVP for the system (34), subject to the initial data

$$\mathbf{U}(r,0)=\mathbf{U}_0(r)=\begin{cases}\mathbf{U}_L+r\,\mathbf{U}'_L\,, & r<0\,,\\ \mathbf{U}_R+r\,\mathbf{U}'_R\,, & r>0\,,\end{cases} \tag{36}$$

where $\mathbf{U}_R$, $\mathbf{U}'_R$, $\mathbf{U}_L$, $\mathbf{U}'_L$ are constant vectors.

The initial structure of the solution $\mathbf{U}(r,t)$ is determined by the limiting values (at $r=0\pm$) $\mathbf{U}_R$, $\mathbf{U}_L$. We therefore associate with the GRP its "limiting planar problem".

Definition 7.1. The "Associated Riemann Problem" (to the GRP with initial data (36)) is the Riemann problem (for the planar system obtained by setting $A(r)=A(0)$), subject to the piecewise constant initial data

$$\mathbf{U}^A_0(r)=\begin{cases}\mathbf{U}_L\,, & r<0\,,\\ \mathbf{U}_R\,, & r>0\,.\end{cases} \tag{37}$$

We denote by $\mathbf{U}^A(r,t)=\mathbf{R}^A\big(\frac{r}{t};\mathbf{U}_L,\mathbf{U}_R\big)$ the solution to the associated problem. Observe that it is "self-similar", depending only on the direction $\frac{r}{t}$.

A schematic description of $\mathbf{U}(r,t)$, $\mathbf{U}^A(r,t)$ is given in Figs. 5(a), (b) respectively.

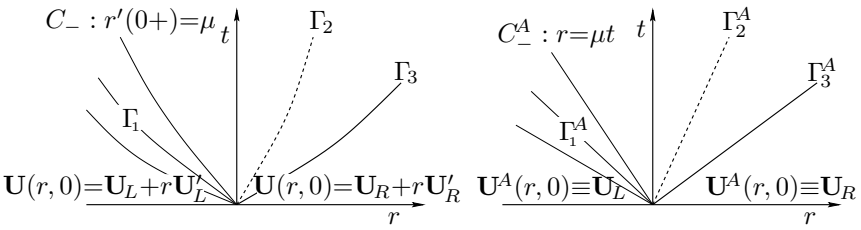

(a) The solution $\mathbf{U}$ (b) The solution $\mathbf{U}^A$

Fig. 5. The solutions to the GRP (a), and its associated RP (b).

It should be emphasized that the solutions are shown only for a short time t, following the "decomposition" of the initial discontinuity at r=0. The waves (in terms of type and initial strength) emanating from that discontinuity are completely determined by the limiting values $\mathbf{U}_R$, $\mathbf{U}_L$ and the planar solution $\mathbf{U}^A$.

The type (shock or CRW – Centered Rarefaction Wave) of Γ_i is identical to that of Γ_i^A. Furthermore, in the shock case (Γ_3, Γ_3^A in Fig. 7) the initial speeds (slopes) and initial jumps of all flow variables are identical. In the case of a CRW the head and tail characteristics (of Γ_1, Γ_1^A in Fig. 7) emanate from r=0 with equal slopes. For any characteristic C_- within the fan Γ_1, approaching the origin with limiting slope μ (see Fig. 7), there is a matching characteristic C_-^A in Γ_1^A whose (constant) slope is μ. Recall that the flow variables along C_- are not constant. However, the limiting values of the flow variables along C_- as $t \to 0$, are equal to the corresponding (constant) values of these variables along C_-^A. Finally, the solution $\mathbf{U}(r,t)$ in the regions between the three waves is smooth and approaches, along any direction r=μt, the corresponding value of $\mathbf{U}^A$, which is constant along the full ray r=μt, t>0. This observation is expressed in the following equation.

$$\lim_{t\to 0+} \mathbf{U}(\mu t, t) = \mathbf{U}^A(\mu t, t) = \mathbf{R}^A\big(\mu; \mathbf{U}_L, \mathbf{U}_R\big) \qquad -\infty < \mu < \infty\,. \tag{38}$$

The smoothness of $\mathbf{U}(r,t)$ (between waves) implies in particular that the wave trajectories (discontinuities, characteristics) are smooth curves.

The solution $\mathbf{U}(r,t)$ can be represented by an asymptotic expansion in terms of r, t. However, here we shall need only the first-order terms of this expansion. (Note that the "zero-order" term is given by Eq. (38).) More explicitly, we need the following.

Definition 7.2. (The Linear GRP).
Given the initial data (36), let $\mathbf{U}(r,t)$ be the solution to the GRP. The Linear GRP is the following. Evaluate the limiting value

$$\left(\frac{\partial}{\partial t}\mathbf{U}\right)_0 = \lim_{t\to 0+} \frac{\partial}{\partial t}\mathbf{U}(0,t)\,. \tag{39}$$

A detailed discussion of the solution to the linear GRP can be found in [2, Chapter 5]. Basically, it builds on the same idea used in the solution to the Riemann problem, i.e., the continuity of the pressure and velocity across the middle (contact discontinuity) wave. This fact implies that although these values vary along the trajectory, their tangential derivatives (as evaluated on the two sides) are identical. This leads to the Main Theorem of Linear GRP as we state below. The simplest (second-order, high-resolution) numerical scheme that can be derived from these considerations is the one based on the Acoustic Approximation . We introduce this approximation and prove the simplified version of the main theorem in this context.

Remark 7.1.

(a) The GRP method is equally applicable to the evaluation of the directional derivative

$$\left(\frac{\partial}{\partial t}\mathbf{U}\right)_{\alpha} = \lim_{t\to 0+} \frac{d}{dt}\mathbf{U}(r{=}\alpha t, t), \qquad -\infty < \alpha < \infty\,. \tag{40}$$

As indicated above, this means that we obtain the full first-order perturbation built into $\mathbf{U}(r,t)$, with respect to the associated $\mathbf{U}^A(r,t)$. This will be important in the application of the GRP numerical method to general "moving grids".

(b) The evaluation of the directional derivatives (40) can be extended to higher-order derivatives, using the same methodology. However the entire numerical treatment presented here is based solely on the linear GRP, combining the simplicity of the algorithm with its high-resolution capability.

It turns out that the most convenient way of dealing with the derivatives along the contact discontinuity is by rewriting the flow equations in a Lagrangian framework. Defining the Lagrangian coordinate ξ by

$$\xi = \int_0^r A(s)\rho(s,0)\,ds\,, \tag{41}$$

the system (34) is replaced by

$$\frac{\partial}{\partial t}\mathbf{V} + \frac{\partial}{\partial \xi}\left(A\mathbf{\Phi}(\mathbf{V})\right) + A\frac{\partial}{\partial \xi}\mathbf{\Psi}(\mathbf{V}) = \mathbf{0}\,,$$

$$\mathbf{V} = \begin{bmatrix}\tau\\ u\\ E\end{bmatrix}, \quad \mathbf{\Phi}(\mathbf{V}) = \begin{bmatrix}-u\\ 0\\ pu\end{bmatrix}, \quad \mathbf{\Psi}(\mathbf{V}) = \begin{bmatrix}0\\ p\\ 0\end{bmatrix}, \tag{42}$$

where it is understood that all flow variables, as well as the coordinate r, are functions of ξ, t. In particular, $A = A(r(\xi,t))$, and the three unknown flow variables $\mathbf{V} = (\tau, u, E)$ now replace those of the Eulerian representation $\mathbf{U} = (\rho, \rho u, \rho E)$, where $\tau{=}1/\rho$. Since $\xi{=}0$ at the initial discontinuity, the contact discontinuity Γ_2 stays along $\xi{=}0$ for $t{>}0$. The wave pattern for the solution to the GRP in (ξ, t) coordinates (analogous to the one depicted in Fig. 5(a)) is schematically given in Fig. 7.

Observe that the limiting values $\mathbf{V}_L$, $\mathbf{V}_R$ are related to $\mathbf{U}_L$, $\mathbf{U}_R$, respectively, as indicated above. The linear initial data (36) are replaced by the

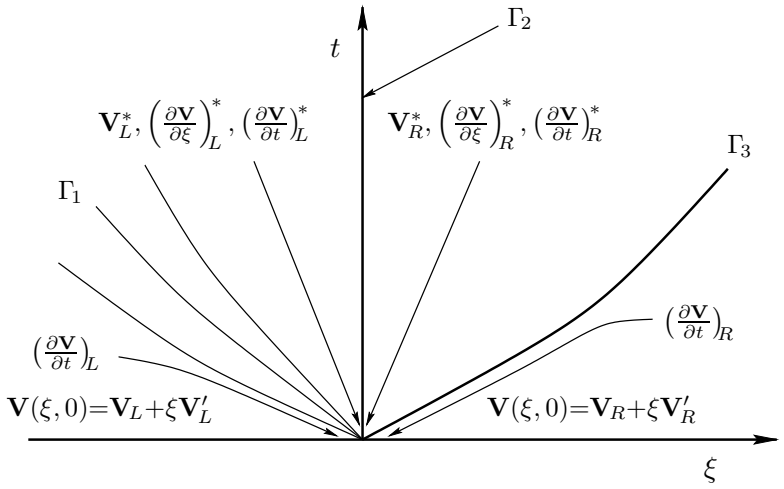

Fig. 6. Structure of the solution to the GRP in Lagrangian coordinates.

linear (in ξ) initial data

$$\mathbf{V}(\xi,0)=\mathbf{V}_0(\xi)=\begin{cases}\mathbf{V}_L+\xi\,\mathbf{V}_L'\,, & \xi<0\,,\\ \mathbf{V}_R+\xi\,\mathbf{V}_R'\,, & \xi>0\,.\end{cases} \tag{43}$$

This is justified as follows. Let Q be any flow variable (say $Q{=}\rho$, or $Q{=}u$). The initial value $Q(r,0)$ is linear (say for $r{>}0$), and using the definition of the Lagrangian coordinate we get

$$\frac{\partial}{\partial\xi}Q(\xi,0)\Big|_{\xi=0+}=[A(0)\rho_{_R}]^{-1}\,\frac{\partial}{\partial r}Q(r,0)\Big|_{r=0+}\,. \tag{44}$$

In this equation we are using $\frac{\partial}{\partial\xi}\Big|_{\xi=0+}$, $\frac{\partial}{\partial r}\Big|_{r=0+}$ to denote the one-sided (from the right) derivatives, and $\rho_{_R}{=}\rho(0+,0)$ to denote the value of the density in $\mathbf{U}_R$ (i.e., the limiting value of $\rho(r,0)$ as $r\to 0+$). Clearly, if $Q(r,0)$ is linear, $Q(\xi,0)$ is generally not linear (in ξ). However, the solution to the linear GRP, as we shall see, depends only on the limiting slopes $\frac{\partial}{\partial\xi}Q(\xi,0)\Big|_{\xi=0\pm}$. Thus, we are justified in assuming that $\mathbf{V}_0(\xi)$ is given by (43), where the relation of $\mathbf{U}_R'$ to $\mathbf{V}_R'$ is obtained from (44). Similarly, the left-hand side derivatives are given by

$$\frac{\partial}{\partial\xi}Q(\xi,0)\Big|_{\xi=0-}=[A(0)\rho_{_L}]^{-1}\,\frac{\partial}{\partial r}Q(r,0)\Big|_{r=0-}\,, \tag{45}$$

for any flow variable Q. Note that the cross-sectional area $A(r)$ is assumed to be continuous (and even continuously differentiable) at all points, including r=0.

We denote by $\mathbf{V}(\xi,t)$ the solution to the GRP (in Lagrangian coordinates) subject to the initial data (43). The associated Riemann solution (Definition 7.1) $\mathbf{V}^A(\xi,t)=\mathbf{R}^A\big(\frac{\xi}{t};\mathbf{V}_L,\mathbf{V}_R\big)$ depends only on ξ/t. As in the Eulerian case, the solution $\mathbf{V}^A$ is the "limit of $\mathbf{V}$" as $t\to 0$ (see (38)). In particular, it will be useful to denote by $\mathbf{V}_L^*$, $\mathbf{V}_R^*$ the (constant) values of the solution along the two sides of the contact discontinuity (compare Fig. 7)

$$\mathbf{V}_L^*=\mathbf{V}^A(0-,t),\qquad \mathbf{V}_R^*=\mathbf{V}^A(0+,t)\,. \tag{46}$$

Clearly, in the case of the pressure and the velocity $p_L^*{=}p_R^*{=}p^*$, $u_L^*{=}u_R^*{=}u^*$. The linear GRP in this framework is transformed into the problem of evaluating the instantaneous time derivatives

$$\left(\frac{\partial}{\partial t}\mathbf{V}\right)^*=\lim_{t\to 0+}\frac{\partial}{\partial t}\mathbf{V}(0,t)\,, \tag{47}$$

along the contact discontinuity ξ=0. The determination of all other directional derivatives (and in particular $\big(\frac{\partial}{\partial t}\mathbf{U}\big)_0$ along r=0), is then straightforward.

Let $\lambda=A'(0)/A(0)$. It measures the deviation of the cross-section from the planar (uniform) case, and plays an important role in the treatment of the GRP.

The main ingredient in the solution of the linear GRP and, indeed, the fundamental building block of the GRP method, is the following theorem.

Theorem 7.1. (Main theorem of linear GRP).
Let $\left(\frac{\partial u}{\partial t}\right)^*$, $\left(\frac{\partial p}{\partial t}\right)^*$, be the time-derivatives of the velocity and pressure along the contact discontinuity, evaluated at t=0+. These derivatives are determined by a pair of linear equations

$$a_{\scriptscriptstyle L}\left(\frac{\partial u}{\partial t}\right)^*+b_{\scriptscriptstyle L}\left(\frac{\partial p}{\partial t}\right)^*=d_{\scriptscriptstyle L}\,, \tag{7.13}$$

$$a_{\scriptscriptstyle R}\left(\frac{\partial u}{\partial t}\right)^*+b_{\scriptscriptstyle R}\left(\frac{\partial p}{\partial t}\right)^*=d_{\scriptscriptstyle R}\,. \tag{7.13}$$

The coefficients depend on the equation of state,
and in addition

$$\begin{array}{lll} a_{\scriptscriptstyle L},\,b_{\scriptscriptstyle L},\,d_{\scriptscriptstyle L} & \textit{depend on} & \lambda,\,\mathbf{V}_L^*,\,\mathbf{V}_L,\,\mathbf{V}_L' \\ a_{\scriptscriptstyle R},\,b_{\scriptscriptstyle R},\,d_{\scriptscriptstyle R} & \textit{depend on} & \lambda,\,\mathbf{V}_R^*,\,\mathbf{V}_R,\,\mathbf{V}_R' \end{array}$$

All six coefficients can be explicitly evaluated from the indicated data.

Remark 7.2. Note that equations $(48)_{L,R}$ are coupled only through the dependence of all six coefficients on the associated Riemann solution $\mathbf{V}^*$. Apart from that, the "left" (resp. "right") coefficients a_L, b_L, d_L (resp. a_R, b_R, d_R) depend only on the "left-side" (resp. "right-side") initial data.

The proof of Theorem 7.1 is rather long and requires the treatment of a centered rarefaction wave in the GRP setting. We refer to[2] for details. However, we shall present here a simplified treatment, which indeed leads to a very successful, easy to implement, second-order numerical scheme.

The Acoustic Case

Assume that the initial flow variables are all continuous at ξ=0 so that $\mathbf{V}_L$=$\mathbf{V}_R$, but we allow jumps in their slopes $\mathbf{V}'_L \neq \mathbf{V}'_R$. Clearly, the associated Riemann solution is now constant

$$\mathbf{V}^A(\xi, t) \equiv \mathbf{V}_L = \mathbf{V}_R \,,$$

hence the GRP solution $\mathbf{V}(\xi, t)$ is continuous at ξ=t=0. It follows that the initial wave pattern of $\mathbf{V}(\xi, t)$ does not contain a jump discontinuity (shock or contact), nor does it contain a CRW. The "waves" emanating from the origin are therefore just characteristic curves C_-, C_+ as in Fig. 7 (the curve C_0 coincides with the particle path ξ=0). These curves are characterized

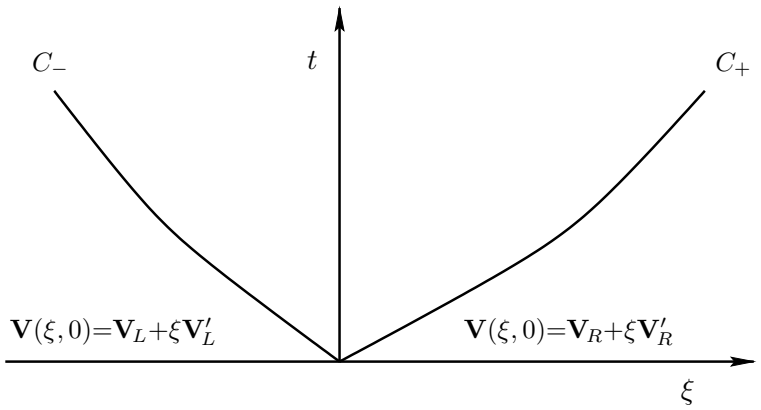

Fig. 7. The "acoustic case" $\mathbf{V}_L$=$\mathbf{V}_R$, $\mathbf{V}'_L \neq \mathbf{V}'_R$.

as "sound waves", justifying the terminology "acoustic case" used here.

Their slopes are $-A(0)g_L = -A(0)\rho_L c_L$ (for C_-) and $A(0)g_R = A(0)\rho_R c_R$ (for C_+), where c_L, c_R are the initial speeds of sound (in the Eulerian frame), as $r \to 0-$, $0+$ respectively. When viewed from the side of the contact discontinuity, these slopes are, respectively, $-A(0)g_L^*$ and $A(0)g_R^*$. Of course, these values are equal to the previous ones, since $\mathbf{V}^* = \mathbf{V}_L = \mathbf{V}_R$. However, we retain the two-sided notation (like g_L, g_L^*, g_R, g_R^* which are all equal) in the formulas. This will enable us to use them in the numerical application based on the acoustic case where $\mathbf{V}_L \neq \mathbf{V}_R$, but their difference is sufficiently "small". It can be shown that the coefficients depend continuously on $\mathbf{V}_L$, $\mathbf{V}_R$.

Proposition 7.1. (The acoustic case – Lagrangian framework).
Assume $\mathbf{V}_L = \mathbf{V}_R$, $\mathbf{V}_L' \neq \mathbf{V}_R'$. *Then the coefficients in Eqs. (48)$_{L,R}$ are given by*

$$a_L = 1,\ b_L = (g_L^*)^{-1} = (\rho_L^* c_L^*)^{-1}, \quad d_L = -(g_L^*)^{-1} g_L \left\{A(0)[g_L u_L' + p_L'] + \lambda u_L c_L\right\}, \tag{49}$$

$$a_R = -1,\ b_R = (g_R^*)^{-1} = (\rho_R^* c_R^*)^{-1}, \quad d_R = -(g_R^*)^{-1} g_R \left\{A(0)[g_R u_R' - p_R'] + \lambda u_R c_R\right\}.$$

In particular, these coefficients depend only on the initial data (including speed of sound).

Note that the derivatives in d_L, d_R are the ξ-derivatives (conforming with the notation $\mathbf{V}_L'$, $\mathbf{V}_R'$). Using (45) we get, for example,

$$u_L'^{-1}\rho_L^{-1}\left.\frac{\partial}{\partial r}u(r,0)\right|_{r=0-}.$$

proof (of Proposition 7.1).
Since u, p are continuous across the line $\xi=0$, the same holds true for their time derivatives $\frac{\partial u}{\partial t}$, $\frac{\partial p}{\partial t}$. They are therefore continuous in the full domain between C_- and C_+ (see Fig. 7) and approach, respectively, $\left(\frac{\partial u}{\partial t}\right)^*$, $\left(\frac{\partial p}{\partial t}\right)^*$ as $(\xi,t) \to (0,0)$ in this domain. In view of the second equation in (42) the derivative $\frac{\partial p}{\partial \xi}$ is also continuous in this domain, and approaches the value $A(0)\left(\frac{\partial p}{\partial \xi}\right)^* = -\left(\frac{\partial u}{\partial t}\right)^*$ as $(\xi,t) \to (0,0)$. The pressure is also continuous across C_-, hence the same is true for its derivative $\frac{dp}{dt}$ (along C_-). Using the chain rule, we can express this derivative in two ways, approaching C_- from either side. For $t \to 0+$, we record separately the two limiting values of the slope as $-A(0)g_L$ and $-A(0)g_L^*$, and obtain

$$\left(\frac{\partial p}{\partial t}\right)^* - A(0)g_L^*\left(\frac{\partial p}{\partial \xi}\right)^* = \left(\frac{\partial p}{\partial t}\right)_L - A(0)g_L p_L'. \tag{50}$$

The flow is isentropic along ξ=*const.* so that

$$\left(\frac{\partial p}{\partial t}\right)_L = c_L^2 \left(\frac{\partial \rho}{\partial t}\right)_L = -g_L^2 \left(\frac{\partial \tau}{\partial t}\right)_L = -g_L^2 \left(Au\right)'_L \,, \tag{51}$$

where in the last step we have used the first equation in (42). We now observe that,

$$\left(Au\right)'_L = \frac{d}{d\xi}\left[A(r(\xi,0))u(\xi,0)\right]_{\xi=0-} = \lambda \rho_L^{-1} u_L + A(0)u'_L \,, \tag{52}$$

and inserting this in (51) yields

$$\left(\frac{\partial p}{\partial t}\right)_L = -\lambda g_L c_L u_L - A(0) g_L^2 u'_L \,. \tag{53}$$

Using (53) and $A(0)\left(\frac{\partial p}{\partial \xi}\right)^* = -\left(\frac{\partial u}{\partial t}\right)^*$ in (50) we get,

$$g_L^* \left(\frac{\partial u}{\partial t}\right)^* + \left(\frac{\partial p}{\partial t}\right)^* = -A(0) g_L^2 u'_L - A(0) g_L p'_L - \lambda g_L c_L u_L$$

which is identical to $(7.13)_L$ with a_L, b_L, d_L as in (49).

The values of a_R, b_R, d_R in (49) are obtained in exactly the same way (or by using the previous argument for the transformed setting $r \to -r$, $\xi \to -\xi$, $u \to -u$, $p \to p$). □

Remark 7.3. Once the time derivative $\left(\frac{\partial p}{\partial t}\right)^*$ is known, the time-derivatives for the density are given by

$$\left(\frac{\partial \rho}{\partial t}\right)^*_{L,R} = (c^*)^{-2}_{L,R} \left(\frac{\partial p}{\partial t}\right)^* \,. \tag{54}$$

The density is evidently continuous across ξ=0 when $\mathbf{V}_L$=$\mathbf{V}_R$. However, Eq. (54) is used in the more general setting as discussed in the paragraph preceding Proposition 7.1.

Remark 7.4. It has been our experience that the acoustic case (i.e., the coefficients as given in (49)) is fully adequate for the numerical simulation of practically all compressible flow problems. The versions of the GRP method based on this observation (labeled E_1, L_1), combine simplicity with accuracy in resolving sharply flow discontinuities ("high-resolution" property).

8. The GRP Numerical Method for Quasi 1-D Compressible Inviscid Flow

The previous section dealt with the solution to the linear GRP. Given initial piecewise linear data, we can find the value of the solution (to the system (34)) and its time-derivative at the singularity. In this section we show how to implement this solution in the design of a suitable numerical scheme, and in fact a group of such schemes.

The schemes based on the GRP methodology range from the very basic one, which is just a straightforward, easy to implement, extension of the classical Godunov scheme, to the "Full GRP" scheme, which requires the full power of the GRP analysis. However, we emphasize that, in all cases, the schemes are based on explicit formulas, derived on the basis of the Riemann solution and the equation of state. Once these formulas are incorporated into the numerical fluxes, the schemes prove to be robust and no intricate post-processing procedures are needed (except for a simple "slope-limiter"). The basic methodology has already been introduced in Section 2. Taking for simplicity a uniform spatial grid $r_j = j\Delta r$, $-\infty < j < \infty$, and uniformly spaced time levels $t_{n+1} = t_n + k$, $t_0 = 0$, we refer to the interval $(r_{j-1/2}, r_{j+1/2})$ as "cell j" and to its endpoints as the "cell boundaries".

At the time level t_n, the solution to (34) in cell j is approximated by an average $\mathbf{U}_j^n$. We advance the averages $\left\{\mathbf{U}_j^n\right\}_j$ to the next time level by a general ("quasi-conservative") scheme

$$\mathbf{U}_j^{n+1} = \mathbf{U}_j^n - \frac{\Delta t}{(\Delta v)_j}\left[A(r_{j+1/2})\mathbf{F}_{j+1/2}^{n+1/2} - A(r_{j-1/2})\mathbf{F}_{j-1/2}^{n+1/2}\right] - \frac{\Delta t}{\Delta r}\left[\mathbf{G}_{j+1/2}^{n+1/2} - \mathbf{G}_{j-1/2}^{n+1/2}\right], \quad (55)$$

where $(\Delta v)_j = \int_{r_{j-1/2}}^{r_{j+1/2}} A(r)\,dr$ is the volume of the duct segment in cell j.

The scheme (55) is a "finite volume" scheme. It is obtained by integrating the quasi-conservation law (34) (after multiplication by $A(r)$) over the space–time rectangle $(r_{j-1/2}, r_{j+1/2}) \times (t_n, t_{n+1})$. The integral $\int_{r_{j-1/2}}^{r_{j+1/2}} A(r)\mathbf{U}(r,t_n)\,dr$ is approximated by $\mathbf{U}_j^n(\Delta v)_j$, and similarly for $t = t_{n+1}$. The integral $\int_{r_{j-1/2}}^{r_{j+1/2}} A(r)\frac{\partial}{\partial r}\mathbf{G}(\mathbf{U}(r,t))\,dr$ is approximated

by $\frac{(\Delta v)_j}{\Delta r}\left[\mathbf{G}\left(\mathbf{U}(r_{j+1/2},t)\right)-\mathbf{G}\left(\mathbf{U}(r_{j-1/2},t)\right)\right]$. The "side" integrals

$$\int_{t_n}^{t_{n+1}} A(r_{j\pm1/2})\mathbf{F}\left(\mathbf{U}(r_{j\pm1/2},t)\right)\,dt\,, \qquad \int_{t_n}^{t_{n+1}} \mathbf{G}\left(\mathbf{U}(r_{j\pm1/2},t)\right)\,dt$$

are then approximated, respectively, by

$$A(r_{j\pm1/2})\mathbf{F}^{n+1/2}_{j\pm1/2}\,\Delta t\,, \qquad \mathbf{G}^{n+1/2}_{j\pm1/2}\,\Delta t\,, \tag{56}$$

which need to be determined. In fact, their evaluation in terms of the data $\left\{\mathbf{U}^n_j\right\}_j$ is what is commonly referred to as the "design of a scheme".

Definition 8.1. The terms $\mathbf{F}^{n+1/2}_{j\pm1/2}$, $\mathbf{G}^{n+1/2}_{j\pm1/2}$ are called the "numerical fluxes" for the quasi-conservative scheme (55).

We shall always assume that the CFL condition is satisfied in the sense that no wave issuing from a singularity $r_{j+1/2}$ at time $t{=}t_n$ reaches the adjacent cell boundaries $r_{j-1/2}$, $r_{j+3/2}$ during the time interval (t_n, t_n+k). In practice, this is achieved by inspecting all such waves at time $t{=}t_n$ and taking their maximal speed S_n. Since (generally speaking) the wave speeds vary in time, an additional "safety" factor $\mu_{CFL}{<}1$ is added to make up for a possible growth of the maximal speed. This factor is then labeled "CFL-ratio", and the next time step k_n is set to be $k_n=\mu_{CFL}\cdot\frac{\Delta r}{S_n}$. For notational simplicity we omit henceforth the dependence of k on n, and write $k_n{=}k$.

The Godunov Scheme

Given the initial data $\mathbf{U}_0(r)=\mathbf{U}(r,0)$, we define the initial set of cell averages by

$$\mathbf{U}^0_j=\frac{1}{(\Delta v)_j}\int_{r_{j-1/2}}^{r_{j+1/2}} A(r)\mathbf{U}_0(r)\,dr\,, \qquad -\infty<j<\infty\,. \tag{57}$$

Next we assume that the cell averages $\left\{\mathbf{U}^n_j\right\}_j$ are known and determine the numerical fluxes in (55). To this end we assume that the cross-sectional area is "locally uniform" in adjacent cells. The system (34) is then transformed into a "planar" one near the cell boundaries $r_{j\pm1/2}$. We further assume that the flow distribution is piecewise (or "cellwise") constant, being equal to $\mathbf{U}^n_j$ throughout cell j (at time $t{=}t_n$). These assumptions imply that, due to the CFL condition, the solution in the time interval (t_n, t_n+k) consists of a "sequence of Riemann solutions". Each cell boundary $r_{j+1/2}$ carries an

initial discontinuity, separating two constant states $\mathbf{U}_L = \mathbf{U}_j^n$, $\mathbf{U}_R = \mathbf{U}_{j+1}^n$. Translating the point $r = r_{j+1/2}$ to the origin, we conclude that the solution along the line $r = r_{j+1/2}$ is constant and equal to the Riemann solution $\mathbf{R}(0; \mathbf{U}_j^n, \mathbf{U}_{j+1}^n)$. The CFL restriction on k prevents the waves emanating from $r_{j+1/2}$ from reaching either $r_{j-1/2}$ or $r_{j+3/2}$, as seen in Fig. 8.

Definition 8.2. (The Godunov Scheme).
Given the initial distribution $\left\{\mathbf{U}_j^0\right\}_{-\infty<j<\infty}$, determine successively (for $n = 1, 2, \dots$) the cell averages by

$$\mathbf{U}_j^{n+1} = \mathbf{U}_j^n - \frac{k}{(\Delta v)_j}\left[A(r_{j+1/2})\mathbf{F}_{j+1/2}^{G,n+1/2} - A(r_{j-1/2})\mathbf{F}_{j-1/2}^{G,n+1/2}\right] - \frac{k}{\Delta r}\left[\mathbf{G}_{j+1/2}^{G,n+1/2} - \mathbf{G}_{j-1/2}^{G,n+1/2}\right] , \qquad -\infty < j < \infty , \quad (58)$$

where the numerical fluxes satisfy,

$$\mathbf{F}_{j+1/2}^{G,n+1/2} = \mathbf{F}\left(\mathbf{R}(0; \mathbf{U}_j^n, \mathbf{U}_{j+1}^n)\right) \qquad -\infty < j < \infty , \quad (59)$$

$$\mathbf{G}_{j+1/2}^{G,n+1/2} = \mathbf{G}\left(\mathbf{R}(0; \mathbf{U}_j^n, \mathbf{U}_{j+1}^n)\right)$$

($\mathbf{F}(\mathbf{U})$, $\mathbf{G}(\mathbf{U})$ as in (34)).

The Basic GRP Scheme

We have seen in the case of the Guckenheimer equation that the Godunov scheme performed reasonably well in capturing jump discontinuities. However, the excessive "dissipativity" of the scheme tends to "spread out" discontinuities and to "clip out" extremal points. These numerical effects are even more pronounced in the case of systems. The remedy suggested in Section 2 was based on the fundamental observation by van Leer:[27] Replace the

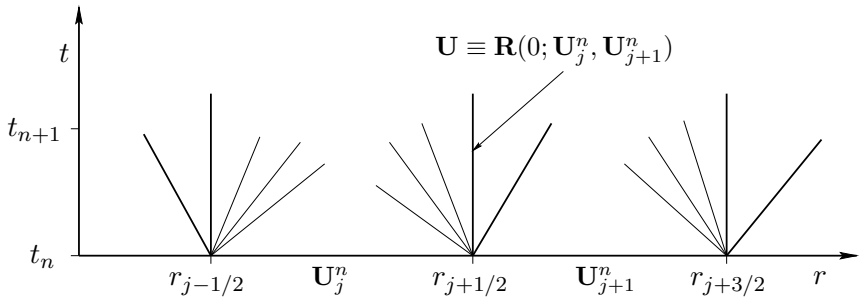

Fig. 8. Structure of the solution for Godunov's scheme.

cellwise constant distribution of variables at time $t{=}t_n$ by a "piecewise linear" distribution, thus achieving second-order accuracy. At the same time, maintaining the "upwind" character of the scheme as in (55) enables the accurate capturing of jump discontinuities. Following this line of thought, we now assume that the flow variables are linearly distributed in each cell, so that at time $t{=}t_n$,

$$\mathbf{U}^n(r) = \mathbf{U}_j^n + (r - r_j)\mathbf{L}_j^n \ , \qquad r_{j-1/2} < r < r_{j+1/2} \ . \tag{60}$$

At the cell boundaries $r_{j\pm 1/2}$ we therefore allow a jump of both the variables and their gradients, as in Fig. 8. The problem is once again to determine

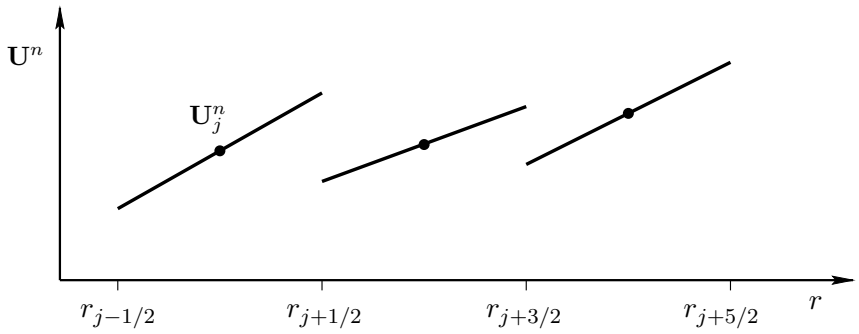

Fig. 9. Distribution of flow variables at time $t{=}t_n$ (GRP setup).

the numerical fluxes as in Definition 8.1. Furthermore, in the case where all slopes $\mathbf{L}_j^n$ vanish and the cross-sectional area is (locally) uniform, we require that the fluxes coincide with those of the Godunov scheme (59).

The reasoning employed in the case of the Godunov scheme can be implemented here. The CFL condition implies that during the time interval $(t_n, t_n + k)$ the exact solution $\mathbf{U}(r,t)$ to the system (34), subject to initial data $\mathbf{U}^n(r)$, is not affected (along the line $r{=}r_{j+1/2}$) by waves issuing from the neighboring discontinuities at $r_{j-1/2}$, $r_{j+3/2}$. Shifting $r{=}r_{j+1/2}$ to $r{=}0$ and the time t_n to $t{=}0$, we see that the solution $\mathbf{U}(r_{j+1/2}, t)$, $t_n \le t \le t_{n+1}$, is that of the GRP where, as in (36),

$$\begin{aligned} &\mathbf{U}_L = \mathbf{U}_j^n + \frac{\Delta r}{2}\mathbf{L}_j^n \ , \qquad \mathbf{U}_R = \mathbf{U}_{j+1}^n - \frac{\Delta r}{2}\mathbf{L}_{j+1}^n \\ &\mathbf{U}_L' = \mathbf{L}_j^n \ , \qquad\qquad\qquad \mathbf{U}_R' = \mathbf{L}_{j+1}^n \ . \end{aligned} \tag{61}$$

Unlike the case of the Godunov scheme, where the waves emanating from the discontinuities propagate along straight lines (see Fig. 8), these waves

are now typically as shown in Fig. 5(a). The solution $\mathbf{U}(r_{j+1/2},t)$ cannot be obtained exactly and we must resort to appropriate approximations. The basic guideline here is to maintain the second-order accuracy, as in the scalar case. With an eye to a simple second-order extension of the Godunov scheme, we now try to design numerical fluxes based on the GRP solution. The first step is the evaluation of the "instantaneous" values of the solution $\mathbf{U}(r,t)$ at the jump discontinuities $(r_{j+1/2},t_n)$. These values are obtained, in accordance with (38), as Riemann solutions related to the values of $\mathbf{U}^n(r)$ at the cell boundaries. Designating these values as

$$\mathbf{U}^n_{j+1/2,-}=\mathbf{U}^n_j+\frac{\Delta r}{2}\mathbf{L}^n_j\ ,\qquad \mathbf{U}^n_{j+1/2,+}=\mathbf{U}^n_{j+1}-\frac{\Delta r}{2}\mathbf{L}^n_{j+1} \tag{62}$$

(these are $\mathbf{U}_L$, $\mathbf{U}_R$ in (61)) and using the notation of (38) we get,

$$\mathbf{U}^n_{j+1/2}=\lim_{t\to t_n+}\mathbf{U}(r_{j+1/2},t)=\mathbf{R}^A\left(0;\mathbf{U}^n_{j+1/2,-},\mathbf{U}^n_{j+1/2,+}\right)\ . \tag{63}$$

In the following theorem we examine the meaning of "second-order accuracy" in the present context.

Theorem 8.1. (Numerical Fluxes for the Basic GRP Scheme).
Consider the piecewise linear distribution $\mathbf{U}^n(r)$ as in (60). At the point $r_{j+1/2}$ define the values $\mathbf{U}^n_{j+1/2}$ as the Riemann solution (63) and $\left(\frac{\partial}{\partial t}\mathbf{U}^{ac}\right)^n_{j+1/2}$ as the acoustic time-derivative, based on the linear profiles (61) . Define the numerical fluxes by,

$$\begin{aligned}\mathbf{F}^{n+1/2}_{j+1/2}&=\mathbf{F}\left(\mathbf{U}^n_{j+1/2}+\frac{k}{2}\left(\frac{\partial}{\partial t}\mathbf{U}^{ac}\right)^n_{j+1/2}\right)\ ,\\ \mathbf{G}^{n+1/2}_{j+1/2}&=\mathbf{G}\left(\mathbf{U}^n_{j+1/2}+\frac{k}{2}\left(\frac{\partial}{\partial t}\mathbf{U}^{ac}\right)^n_{j+1/2}\right)\ .\end{aligned} \tag{64}$$

Using these fluxes in (55), the resulting scheme is of second-order accuracy.

Definition 8.3. The scheme presented in Theorem 8.1 is the BASIC GRP SCHEME, and we label it the E_1 SCHEME.

Remark 8.1. (The E_1 Scheme as a generalization to Godunov's Scheme). Godunov's scheme serves as the foundation of the E_1 scheme. It carries the main burden of the "upwinding". As a result, it serves as the basis for the "shock capturing" capability of the scheme. The refinement involved in the E_1 scheme contributes to the "high-resolution" (i.e., "sharpness") of the captured discontinuities. Inasmuch as "computation time" is considered,

the construction of the time-derivatives adds, in practical cases only 2–5% to the time required for the computation of the Riemann solution $\mathbf{U}^n_{j+1/2}$. Remark that no information concerning the equation of state is needed for the time-derivatives.

The E_∞ Scheme, Intermediate Schemes, MUSCL

In Theorem 8.1 we defined the numerical fluxes based on the acoustic approximation. However, starting from the piecewise linear distribution (60) we can evaluate, by means of the full solution to the linear GRP, the exact time-derivative $\left(\frac{\partial}{\partial t}\mathbf{U}\right)^n_{j+1/2}$. Equation (64) for the numerical fluxes is then replaced by

$$\begin{aligned}\mathbf{F}^{n+1/2}_{j+1/2} &= \mathbf{F}\left(\mathbf{U}^n_{j+1/2} + \frac{k}{2}\left(\frac{\partial}{\partial t}\mathbf{U}\right)^n_{j+1/2}\right)\ ,\\ \mathbf{G}^{n+1/2}_{j+1/2} &= \mathbf{G}\left(\mathbf{U}^n_{j+1/2} + \frac{k}{2}\left(\frac{\partial}{\partial t}\mathbf{U}\right)^n_{j+1/2}\right)\ .\end{aligned} \tag{65}$$

Definition 8.4. (E_∞ Scheme).
The scheme (55), with numerical fluxes given by (65), is called the E_∞ Scheme.

The reason for the indices in labeling the E_1, E_∞ schemes lies in the order (in k) to which the numerical fluxes are evaluated. In E_∞, they are obtained from the exact solution to the linear GRP, and no approximation is involved (once the linear distributions $\mathbf{U}^n(r)$ are given). On the other hand, in the case of E_1, the numerical fluxes are based on the time-derivative $\left(\frac{\partial}{\partial t}\mathbf{U}^{ac}\right)^n_{j+1/2}$, which approximates the exact solution to the linear GRP only within $O(k)$. By this convention, if the computed time-derivative approximates the exact one $\left(\frac{\partial}{\partial t}\mathbf{U}\right)^n_{j+1/2}$ within $O(k^2)$ error, we refer to the resulting scheme as an E_2 scheme. Such an approximation results if the acoustic approximation is replaced by the assumption that the waves Γ_1, Γ_3 are always SHOCKS satisfying the Rankine-Hugoniot condition. It means that a CRW is replaced by a "rarefaction shock". This assumption and the resulting approximation is the one used by van Leer[27] in his pioneering work.

Concluding the GRP Algorithm

We can now sum up the GRP algorithm, which is a second-order upwind finite-difference scheme for the system (34) governing quasi 1-D compressible flow. Referring to this system, the vector of unknown flow variables is

$$\mathbf{U} = \begin{bmatrix} \rho \\ \rho u \\ \rho E \end{bmatrix} .$$

At the cell boundaries $\left\{r_{j+1/2}\right\}$ we obtain the values $\left\{\mathbf{U}^n_{j+1/2}\right\}$ by solving a (planar) Riemann problem. Next we evaluate the "instantaneous" time-derivatives $\left(\frac{\partial}{\partial t}\mathbf{U}^{app}\right)^n_{j+1/2}$. They are computed by the acoustic approximation or by the analytic solution to the linear GRP (or any intermediate scheme). The numerical fluxes are given by

$$\begin{aligned} \mathbf{F}^{n+1/2}_{j+1/2} &= \mathbf{F}\left(\mathbf{U}^n_{j+1/2} + \frac{k}{2}\left(\frac{\partial}{\partial t}\mathbf{U}^{app}\right)^n_{j+1/2}\right), \\ \mathbf{G}^{n+1/2}_{j+1/2} &= \mathbf{G}\left(\mathbf{U}^n_{j+1/2} + \frac{k}{2}\left(\frac{\partial}{\partial t}\mathbf{U}^{app}\right)^n_{j+1/2}\right), \end{aligned} \tag{66}$$

and the new values $\left\{\mathbf{U}^{n+1}_j\right\}$ by (55). The new cell boundary values $\left\{\mathbf{U}^{n+1}_{j+1/2}\right\}$ are determined by using the linear approximation (in time) at the cell boundaries and the new slopes $\left\{\mathbf{L}^{n+1}_j\right\}$ by differencing these values.

Finally, the slopes in all cells are subjected to a "slope limiter" algorithm, without EVER changing the average values $\left\{\mathbf{U}^{n+1}_j\right\}$. The fact that slope-limiting is indispensable has already been demonstrated in the scalar case above. In practice, each of the three basic flow variables is subjected to the same simple algorithm used in the scalar case.

9. Fluid Dynamical Examples

Various studies on shock wave phenomena have been conducted in the course of implementing the GRP scheme to the fluid dynamical equations, some of them including comparison to experiments involving complex wave interactions. Here we consider specifically the four cases :

- A rarefaction wave propagating into a narrower duct via a converging nozzle.
- Shock diffraction by a square cavity.

- Second reflection of a shock wave by a double wedge.
- Lagrange–Euler coupled flow of heterogeneous gas–grain mixture.

In all but the first example a comparison to experimental observation is included.

9.1. *Wave Dynamics in a Duct with a Converging Segment*

Consider a centered rarefaction wave that propagates in a planar duct comprising two long segments of uniform cross-section area joined by a smooth converging nozzle. This problem serves as a model to processes that take place in diverse systems of industrial and scientific interest, such as internal combustion engines, or turbofan/turbojet engines. In addition to shedding light on the nature of the interaction between a rarefaction wave and a converging nozzle, the significance of this case lies in the comparison we make between a full multi-dimensional solution and the corresponding quasi 1-D approximation. The reason is that the latter (often referred to as the "duct flow" approximation) is commonly employed as an engineering design tool. Hence, studying the bounds of its validity as a simplified approximation to the full multi-dimensional solution is highly significant to engineering design and analysis.

In a study of wave interaction with diverging or converging ducts,[16] it was found out that at large times the solution produced by the quasi 1-D approximation was usually close to the full 2-D solution. This was particularly so in the case of shock waves. However, this is not universally so, and as a specific example of wave interaction where the quasi 1-D solution and the 2-D solution differ, we consider here the case of a 1:10 pressure ratio rarefaction wave in a fluid assumed to be a perfect gas with $\gamma = 1.4$. The CRW is initially located in the wider part of the duct, and it propagates toward a (short) converging nozzle of $2:1$ cross-section area ratio. The initial data is that of a Riemann problem designed to produce a right-propagating CRW. It consists of two uniform states

$$\mathbf{U}(r,0) = \begin{cases} \mathbf{U}_L = [\rho_L, p_L, u_L] = [0.27030, 0.1, -1.4016]\,, & r < 1.3\,, \\ \mathbf{U}_R = [\rho_R, p_R, u_R] = [1.4, 1, 0]\,, & r > 1.3\,. \end{cases} \tag{67}$$

Here we use "r" as the spatial coordinate along the duct axis. The location of the initial discontinuity ($r = 1.3$) is just ahead of the converging segment that occupies the interval $1.6 \le r \le 2.6$. The cross-section area function of

the duct $A(r)$ is given by

$$A(r) = \begin{cases} 2, & r < 1.6\,, \\ 2\exp\left[-\frac{1-cos(\pi(r-1.6))}{2}\ln 2\right], & 1.6 \le r \le 2.6\,, \\ 1, & r > 2.6\,. \end{cases} \tag{68}$$

We assume that the two-dimensional duct is symmetric and its centerline in the (x, y) plane is the x-axis, which coincides with the r-axis. The upper contour of the duct (see Fig. 9.1(a)) is thus $y(x) = \frac{1}{2}A(x)$. Due to the duct symmetry, the 2-D computation is conducted in the upper half of the duct, embedding it in the (finite) rectangular domain $(x, y) \in [-1.6, 9.4] \times [0, 1]$, which is divided into a grid of 550×50 square cells ($\Delta x = \Delta y = 0.02$). The computation is performed by the operator-split 2-D GRP scheme, using the Moving Boundary Tracking (MBT) method [2, Chapters 7,8] to implement the duct wall contour. A rigid-wall boundary condition is also imposed at the centerline ($y = 0$). On the left and right sides of the computational rectangle we impose "non-reflecting" boundary conditions designed to allow waves to pass through these endplanes (almost) undisturbed. The computation was performed in the time interval $[0, 9]$, with time steps adjusted (at each integration cycle) to have a nearly constant CFL coefficient $\mu_{CFL} = 0.7$.

The quasi 1-D computation was conducted in the spatial interval $[-1.6, 9.4]$, which was divided into a grid of 550 cells of equal length $\Delta r = 0.02$. The cross-section area function is $A(r)$ (given in (68)). The boundary conditions at either endpoints were of the same "non-reflecting" type as in the 2-D case. The computation was performed with time steps adjusted to have the same $\mu_{CFL} = 0.7$ and in the same time interval $[0, 9]$.

We now turn to the results of the 2-D computation, shown as a time-sequence maps of isobars ($p = const.$) in Fig. 9.1. When the right-propagating rarefaction wave enters the nozzle (Fig. 9.1 at $t = 1.5$) the fluid in the nozzle is set in motion, gradually evolving into a supersonic expansion flow in a diverging nozzle.[a] The time-sequence of isobars plots (Fig. 9.1), shows that the entire flow field is progressively adjusting to the presence of a diverging nozzle in its midst, in particular by forming an upstream-facing oblique shock wave (marked by $*$ in Fig. 9.1). This shock stabilizes near the duct "corner point", where the flow exits from the nozzle into the wider duct segment. In addition to pressure-matching, the oblique

[a]Note that in the initial state $\mathbf{U}_L$ the flow is already supersonic since $u_L = -1.947 c_L$, i.e., $|u_L| > c_L$.

shock serves to align the velocity of the flow along the diverging nozzle contour with the downstream duct wall. The interaction of the flow with the centerline ($y = 0$) aligns the velocity vector with that boundary, producing the familiar pattern of Mach reflection, where three shock waves intersect at a "triple point" (see Fig. 9.1 at $t = 9$).

In Fig. 9.1 we compare the results of the 2-D and quasi 1-D computations at the final time $t = 9$. First we show the 2-D isobars (Fig. 9.1(a)) as in the last frame of Fig. 9.1. This is followed by profiles of density, pressure, and flow Mach number, as functions of the centerline coordinate (Figs. 9.1(b)–(d)). They are extracted from the 2-D and the quasi 1-D solutions. The 2-D computation results are shown as dashed lines for the flow at the centerline, and dash-dot lines for the flow at the duct wall; the quasi 1-D profiles are shown as solid lines.

It is evident from the comparison (Fig. 9.1) that the two solutions are in close agreement throughout the narrower duct segment ($r > 2.6$), but disagree elsewhere. Also, it is observed that the "transmitted" part of the rarefaction wave propagates almost "one-dimensionally" into the narrow part of the duct (where it naturally agrees well with the corresponding quasi 1-D solution). Moreover, it is interesting to observe that at the entrance to the nozzle ($r = 2.6$), the flow speed is sonic ($M = 1$ in Fig. 9.1(d)). The nozzle flow at large times thus approaches a *steady* supersonic expansion flow, commencing at a virtual sonic plane ("nozzle entrance"), which serves to "match" the *unsteady* rarefaction wave on its right to the steady flow on its left.[b]

In other words, upon passing through the nozzle, the CRW is "truncated" into a "transmitted" part and a "reflected" part, the two being separated by a (nearly) steady flow through the diverging nozzle. With respect to the incident CRW, the first part corresponds to the sector between the leading characteristic $\frac{dr}{dt} = c_R$ and the "sonic characteristic" $\frac{dr}{dt} = u+c = 0$ (which is positioned at the nozzle entrance $r = 2.6$). The second part corresponds to the "tail" sector of the CRW, between the tail characteristic $\frac{dr}{dt} = u_L + c_L < 0$ and an unspecified inner characteristic (it is "unspecified" since here we focus our attention on the other parts of the flow field). The region of "nearly steady" flow comprises the entire diverging nozzle and extends to the left of the shock structure.

Now the source of disagreement between the quasi 1-D and the 2-D

[b]Recall that under the quasi 1-D approximation for steady compressible flow in a Laval nozzle ([21,24]), a supersonic flow in the diverging part of the nozzle is possible only when the fluid enters it (through a minimum-area "throat") at sonic speed.

solutions is evident. The fluid expands as it flows through the nozzle at supersonic speed, and a full 2-D description of this flow involves an oblique shock system at the nozzle exit (Fig. 9.1(a)), which is poorly approximated by the cross-section-averaged quasi 1-D solution that relies on a normal shock for matching the over-expanded supersonic nozzle flow to the pressure ahead.

It is concluded that although quasi 1-D calculations may generally be adequate as an engineering approximation, a verification by comparison to the appropriate multi-dimensional solution is required in order to make sure that the disagreement between the two remains within acceptable bounds. Our test case analysis thus brings out the significance of full multi-dimensional numerical solutions; the (simpler) quasi 1-D solutions may not always serve as adequate approximations.

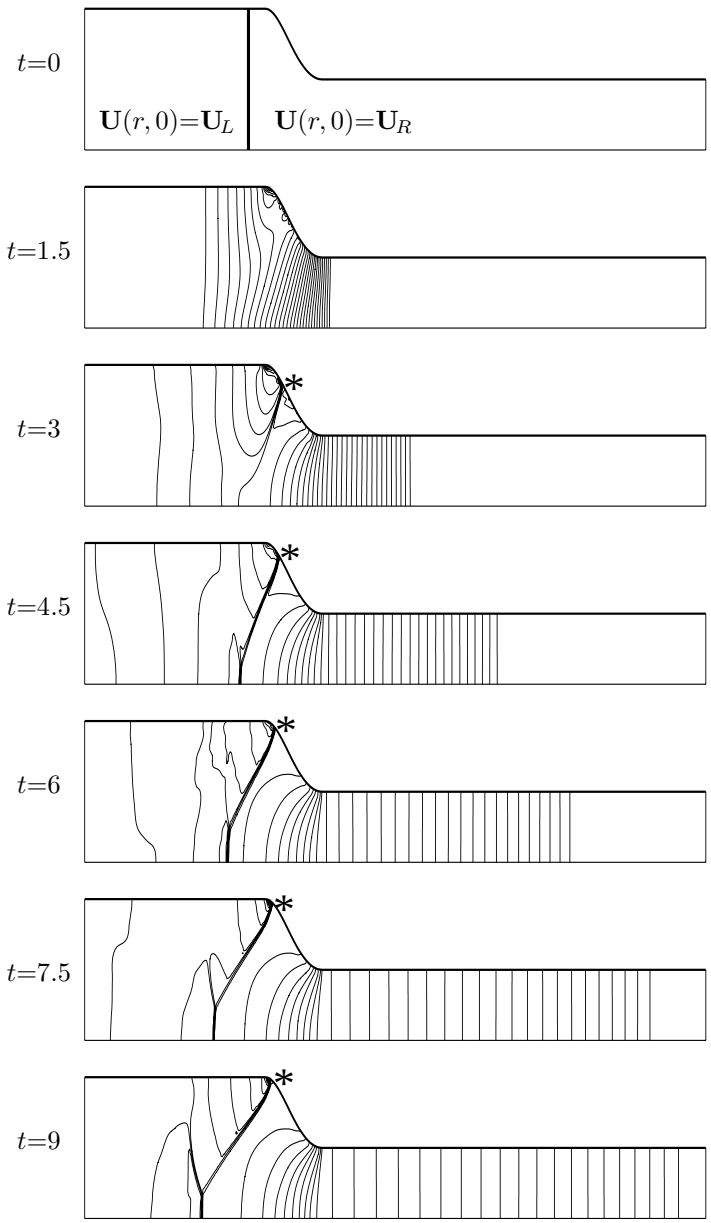

Fig. 10. Time sequence of CRW interaction with a converging segment. Isobars map. The * marks shock formation at duct wall. (Duct width here is twice the true size, for better visibility).

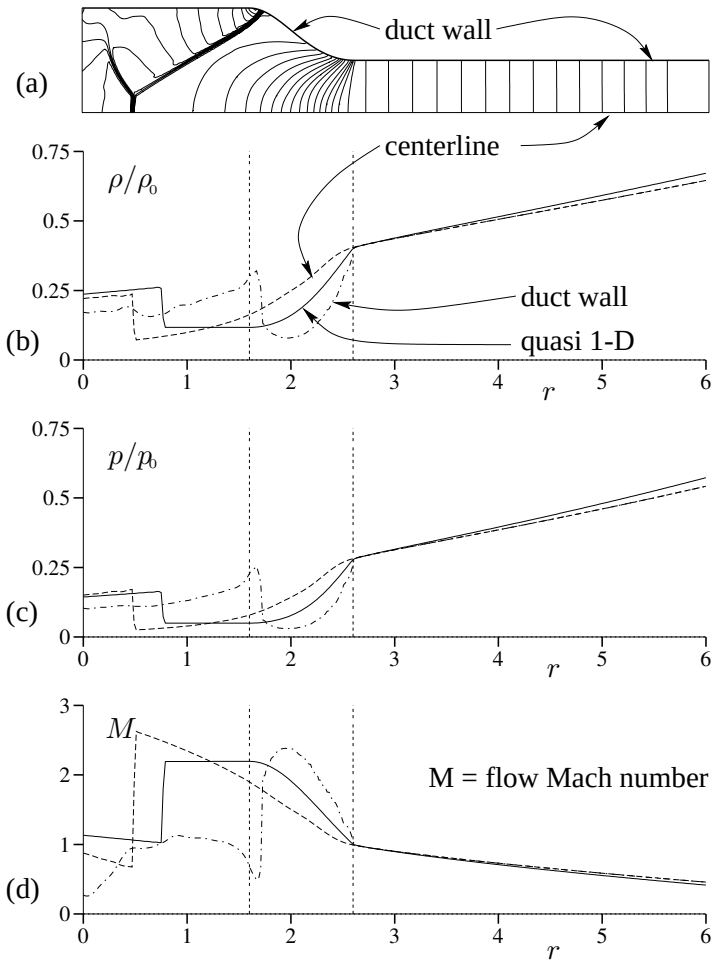

Fig. 11. CRW interaction with a converging segment; comparison of 2-D and quasi 1-D results at time $t = 9$.
(a) Isobars of 2-D calculation.
(b)–**(d)** Quasi 1-D solution. Distribution of density, pressure and flow Mach number (taken as positive).

9.2. *Shock diffraction by a square cavity*

This test case is a genuinely two-dimensional interaction of a planar shock wave with the solid boundaries of a square cavity, where the flow is governed by a combination of diffraction and reflection processes, and the resulting flow field is quite complex. The accuracy of the 2-D operator-split GRP scheme [2, Chapter 7] is demonstrated by the degree of agreement between simulations and experimental shadowgraphs (showing shock or contact discontinuities). For a detailed account of this study we refer the reader to.[15] Here we consider the particular case of an incident shock propagating into still air at Mach number $M_s = 2.032$, and interacting with a $50\,mm$ square cavity. In the experiment the interaction was recorded at an equally-spaced time sequence of shadowgraphs. For a comprehensive presentation of the results of simulations and experiments we refer to the above cited reference. Here we consider just the shadowgraph, taken at $t = 150\mu s$ from the beginning of the interaction.

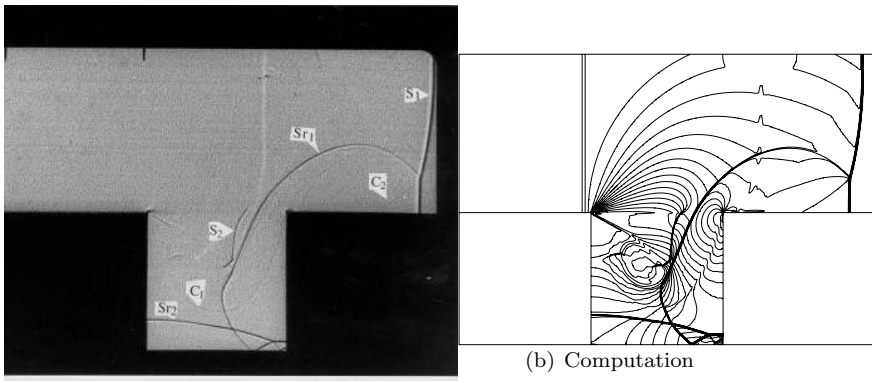

(a) Experiment (b) Computation

Fig. 12. Diffraction of $M_s = 2.032$ shock with a square cavity at time $t = 150\mu s$.

The computational configuration was a rectangle of $220\times110\,mm$, which was divided into a grid of 990×495 square cells (i.e., the cavity was resolved by 225×225 cells). The integration time step was constant $\Delta t = 0.1\,\mu s$, which was verified to yield a CFL ratio $\mu_{_{CFL}}$ of no more than 0.5. The air was assumed to be a perfect gas with $\gamma = 1.40$ and molecular weight of 29.0. In order to increase the efficiency of computation, the E_1 scheme was used at every cell-interface where the solution to the associated Riemann problem involved pressure jumps lower that 1% of the cell pressure (by

monitoring the computations, it was found out that only about 1% of the cell-interfaces required the full GRP solution, i.e., the E_∞ scheme was rarely used). The initial air temperature was $296\,K$.

The results are shown in Fig. 9.2, where various waves are indicated on the shadowgraph. The primary (incident) shock S_1 has developed into a Mach reflection pattern with a triple point, from which the Mach stem extends normally to the wall, the reflected shock Sr_1 curves around the corner, and the slipline (contact discontinuity) C_2 separates the Mach stem from the reflected shock. Another major reflected shock is Sr_2, which is due to reflection from the cavity floor. The shock S_2 is a secondary shock wave, which developed due to over-expansion of the flow around the leading corner (note that the shock at the nozzle exit in the former example is likewise due to flow over-expansion), and the contact discontinuity surface C_1 separates the the flow through the secondary shock from the fluid that was swept by the primary shock.

Thus, the major features of the shock–cavity interaction are well understood in terms of classical fluid dynamics, and moreover, a good agreement between the observed shadowgraph and the computed simulation is obtained. This constitutes a validation of the GRP scheme by demonstrating that it is capable of producing physically accurate simulations of complex shock wave structures, and in particular, it validates the scheme extension to two space dimensions using operator splitting.

Moreover, this physical validation may also be interpreted as leading to interesting conclusions concerning an important mathematical property of the scheme, namely its capability of producing unique entropy solutions. It is well known that weak solutions (i.e., solutions involving shocks or other discontinuities) to the hydrodynamic conservation laws of an inviscid fluid require an additional constraint in order to render them unique and physically correct. This is the so-called "entropy condition", the corresponding solution being referred to as an "entropy solution" (see the discussion of the entropy condition (16) in the case of a scalar equation). The fact that a numerical code produces physically correct simulations of complex shock wave structures supports the contention that its finite-difference scheme converges to an entropy solution.

Similar studies are reported in[17] for a shock wave propagating in a branched duct, and in[14] for the passage of a shock wave through a double-bend duct. In all these studies a remarkably good agreement was obtained between the observed (complex) shock structures and the corresponding GRP simulations.

9.3. *Second reflection of a shock wave by a double wedge*

Here we consider the reflection of a shock wave from a double wedge. The shock is regularly reflected from the first wedge, and the incident–reflected shock pattern is subsequently reflected from the second wedge. In our case the surface of the second wedge is parallel to the incident shock front, as shown in Fig. 9.3. The case considered here is an incident shock propagating

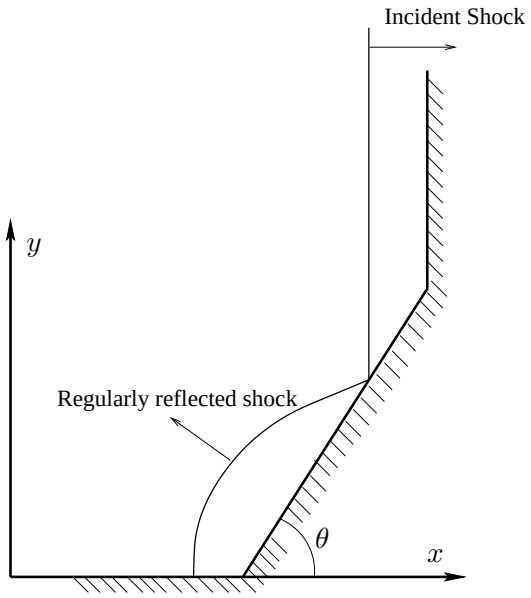

Fig. 13. Regular shock reflection from first wedge.
Incident shock is parallel to second wedge surface.

into still air at a Mach number $M_i = 1.488$. The wedge angle is $\theta = 55°$. For a more detailed account of this study, as well as additional cases of shock Mach number and wedge angle, we refer to.[7]

Since the incident shock is regularly reflected by the wedge surface, the flow is self-similar in a region extending to some finite distance from the point of reflection. In this region the oblique reflected shock is planar. Therefore, the second reflection is also self-similar within some finite region about the second corner. The experimental and computed flow fields are shown as isopycnics (lines of constant density) in Fig. 14 at a time where the pattern due to the second reflection is still self-similar.

The computation domain was the rectangle $[0 < x < 105] \times [0 < y <$

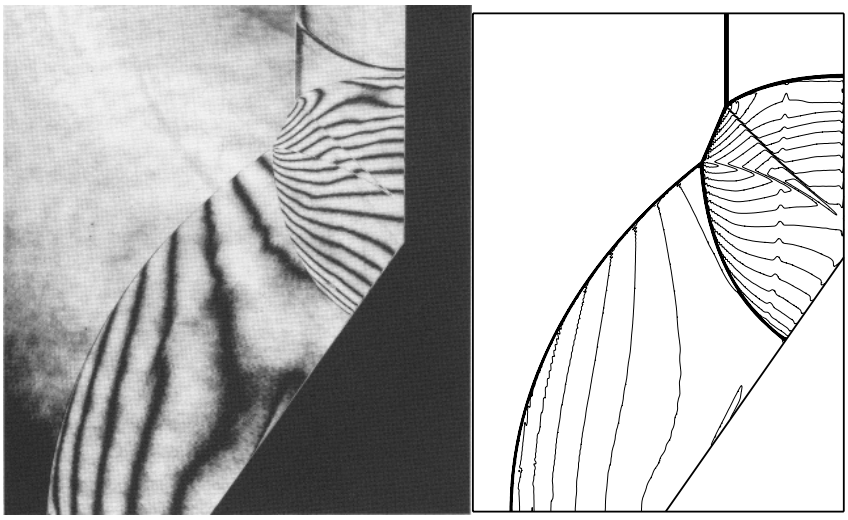

(a) Experimental (b) Computation

Fig. 14. Second reflection of $M_s = 1.488$ shock with a double wedge at time $t = 206$.

141] (dimensions in mm), which was divided into 525×705 square cells. The wedge started at the point $(x, y) = (54.6, 0)$, and it was inclined to the x-axis by an angle $\theta = 55°$. The computation was performed by the Moving Boundary Tracking (MBT) method [2, Chapter 8], where the wedge served as a stationary rigid-wall boundary. A rigid-wall boundary condition was also imposed at all other boundaries of the computation domain, except the edge $x = 0$ where an inflow boundary condition corresponding to the incident shock was imposed. The initial position of the shock was $x = 53.6$, and the fluid state ahead of the shock was $[\rho, p, u]_o = [1.20, 0.0985, 0]$ (in mks units). The fluid was taken as an ideal gas with $\gamma = 1.4$. The integration time step was calculated at each cycle so as to have a CFL ratio of $\mu_{CFL} = 0.7$.

Consider the experimental isopycnics given in Fig. 14(a), and the corresponding computational map in Fig. 14(b). Since the incident shock has already been reflected from the second wedge (which is simply the shock tube endwall), it is seen as a planar shock segment parallel to the endwall. The regularly-reflected curved shock is clearly visible; it is joined to the latter by a short (oblique) shock segment, whose endpoints are in fact "triple points" analogous to the triple point in a Mach reflection. Each one

of these points marks the intersection of three shocks and a slip surface, as is clearly visible on both the experimental and computational maps. The third shock is curved, and is apparently produced by the "secondary" reflection at the wedge corner, which commences when the regular reflection point (see schematic description in Fig. 9.3) arrives at that corner. The agreement between the experimental and computed wave fronts and isopycnic lines is very good. The fact that this complex shock pattern is well captured by the GRP/MBT scheme, may be regarded as a validation of the scheme for shock reflection phenomena.

9.4. *Lagrange–Euler Scheme for a Gas–Grains Mixture*

Here we consider the flow of a heterogeneous mixture comprising (solid) elastic grains immersed in an inviscid compressible fluid (gas). The motion of the grains is coupled to the gas flow through the pressure at the gas–grain interface, and the grains may also interact with each other by collision. We treat the fluid dynamics of this mixture by an original method named LEGS (Lagrange–Euler Granular Simulation), which is in fact a reduced version of the classical CEL (Coupled Euler Lagrange) method due to Noh.[22] The key idea of CEL is to employ a Eulerian description for the gas flow, while handling the (deformable) immersed solid via Lagrangian coordinates. The coupling is achieved by taking the Lagrange boundaries as "moving boundary surfaces" with respect to the gas, then in turn using the computed gas pressure as the "driving force" acting on the Lagrange boundaries. In the following we provide a brief outline of the two-dimensional LEGS scheme, referring to[31] for a more detailed description.

A typical flow setup may consist of several tens or hundreds of grains "floating" in a Cartesian grid, as shown schematically in Fig. 15(a). The grains are assumed to be rectangular, with sides parallel to the Cartesian axes. Thus, the complexity of the Lagrange–Euler coupling algorithm is drastically reduced, enabling the handling of a large number of grains. The fluid dynamical equations are integrated using the operator-split GRP finite-difference scheme, where the integration is performed alternately in the x, y directions. In the treatment of cells intersected by moving grain boundaries we take account of the evolving cell geometry, as in the MBT/GRP scheme [2, Chapter 8]. The grain motion is likewise split into a one-dimensional "x-phase" and a one-dimensional "y-phase", which are performed with the corresponding operator-split integration phases of the Euler equations for the gas. The scheme for the grains is thus not

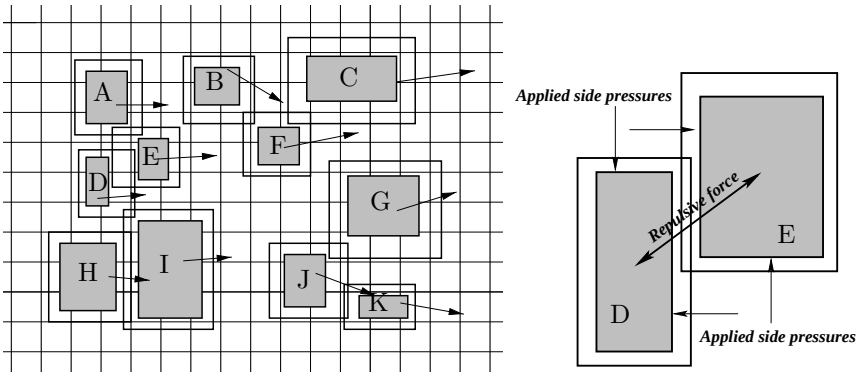

(a) Grain clusters in an Euler grid (b) Repulsive force for pair DE

Fig. 15. Haloed rectangular grains embedded in an Euler grid.

truly two-dimensional; however, it is deemed a reasonable approximation in flows involving a relatively small ("elastic") deformation of the grains. The grains may also exchange momentum by (elastic) collisions. To that end, each grain is surrounded by a narrow "potential halo" (see Fig. 15(a)), where a strong intergranular repulsive potential is invoked whenever grain halos intersect; the potential energy increases sharply as function of the intersection area. This assures that the grains themselves (the gray area in Fig. 9.4) never intersect. The repulsive force is applied per colliding grain pair, and is directed along the line joining the two centers. The force components are represented by a uniform pressure on the "colliding" sides of the grains (two sides per grain); this pressure is added to the gas pressure acting on the respective sides. Referring to the schematic configuration in Fig. 15(a), we see several clusters of grains, such as AEDIH, whose halos intersect. Take for instance grain E; it interacts with grains A and D. So its total intergranular force will be the (vector) sum of the repulsive forces due to the pairs AE and DE. In Fig. 15(b) we show graphically the repulsive force due to the DE pairwise interaction, and the grain sides to which its components are applied as distributed pressures. We point out that, unlike the schematic dimensions in Fig. 15(a), typical grain side lengths are $L = 10 \times a$ and typical halos are $h = a$, where a is the size of an Euler mesh cell.

A physical validation of LEGS was made possible by an experiment due to Rogue et al.,[23] where a granular bed of $2mm$ Nylon spheres is lifted up (and dispersed) by a shock wave in air. The experimental setup consists

of a vertical shock tube (Fig. 16(a)), and the granular bed is made by loosely piling the nylon spheres on a thin-wire screen up to a thickness of $20mm$. The upper end of the tube is open to the atmosphere. An upward-propagating shock wave is generated well below the bed by a diaphragm rupture, releasing high-pressure air (that part of the shock tube is not shown in Fig. 16(a)). When the shock wave arrives at the bed it is simultaneously reflected and transmitted while lifting and dispersing the grains. The gas pressure time history was recorded by two gauges: one located $110mm$ below the screen, the other $43mm$ above the screen.

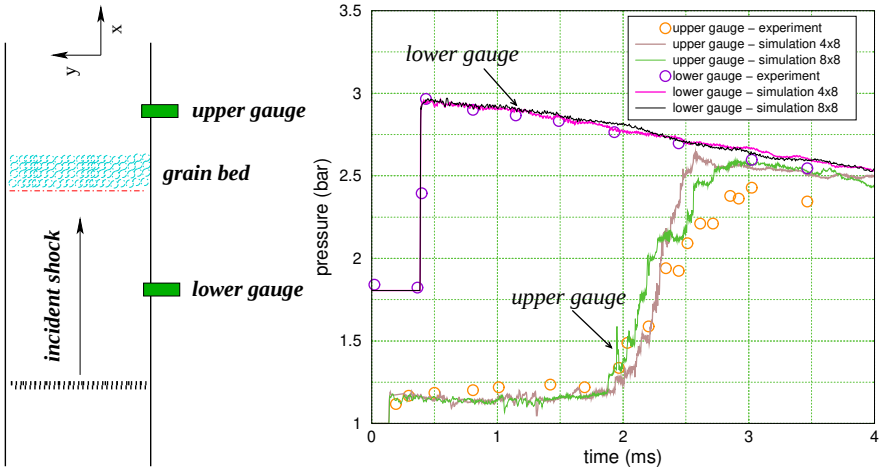

(a) Vertical shock tube (b) Pressure gauge histories

Fig. 16. Interaction of a granular bed with a $M_s = 1.30$ air shock. Bed thickness is $20mm$; loosely-piled $20mm$ nylon spheres.

Turning to the simulation, it is conducted as follows. The computation domain is the rectangle $[0 < x < 600] \times [0 < y < 20]$ which is divided into a grid of 2400×80 square cells (dimensions are in mm). The bottom of the granular bed (the screen in the experiment) is located at $x = 200$. For the initial grain array we divided the square $[200 < x < 220] \times [0 < y < 20]$ into 8×8 square "unit cells" of dimensions 2.5×2.5. A square nylon grain (density 1100, sound speed 1000, in mks units) of size 2×2 (and halo width $h = 0.1mm$) was placed in the middle of each unit cell, so that the grains occupied a fraction of 0.64 of the (2-D) bed volume, compared to a 0.65 fraction estimated for the actual bed by Rogue.[23] Now, in order to somehow account for the asymmetry of the loosely packed bed of spherical

grains, we varied randomly the dimensions of each grain by about $\pm 3\%$, while retaining its correct mass (area). The incident shock was initially placed $1.25mm$ below the bed, and its Mach number was $M_i = 1.30$. The state ahead of the shock was $[\rho, p, u]_o = [1.29, 0.1, 0]$ in mks units, and the air was assumed to be an ideal gas with $\gamma = 1.4$.

It is evident from Fig. 9.4 that there is a very good agreement between the measured and computed pressure history at the lower gauge. The agreement for the upper gauge is not quite as good, probably since it is more dependent on an accurate simulation of the bed spreading, and the resulting influence on the air drag. The fact that the computed pressure is higher than the measured one seems to indicate that the computed drag effects are somewhat undervalued.

We point out that this method is aimed at replacing existing multi-phase methods,[23] which do not achieve any better agreement in this case. Moreover, the multi-phase modeling requires additional information: a drag coefficient for the gas–grain interaction as function of the relative gas–grain flow, and a quite artificial "intergranular stress" (as function of locally-averaged density of grain cluster) in order to account for grain–grain collisions. At present, no better mathematical modeling of heterogeneous gas–grain flow is known. In view of all that, the LEGS approach to the considered class of flows seems quite promising; it is currently being extended to applications involving granular combustion.

References

1. M. Ben-Artzi and J. Falcovitz, *A second-order Godunov-type scheme for compressible fluid dynamics*, Journal of Computational Physics, 55:1–32, 1984.
2. M. Ben-Artzi and J. Falcovitz, *Generalized Riemann problems in computational fluid dynamics*, Cambridge University Press, London, 2003.
3. M. Ben-Artzi, J. Falcovitz, and U. Feldman, *Remarks on high-resolution split schemes computation*, SIAM Journal on Scientific Computing, 22:1008–1015, 2000.
4. M. Ben-Artzi, J. Falcovitz, and J. Li, *Wave interactions and numerical approximation for two-dimensional scalar conservation laws*, Comp. Fluid Dynamics J., 14:401-418, 2006.
5. A. J. Chorin and J. E. Marsden, *A Mathematical Introduction to Fluid Mechanics*, volume 4 of Texts in Applied Mathematics, Springer, New York, second edition, 1990.
6. R. Courant and K. O. Friedrichs, *Supersonic Flow and Shock Waves*. Springer, New York, 1976.
7. J. Falcovitz, G. Alfandary, and G. Ben-Dor, *Numerical simulation of the head-on reflection of a regular reflection*, International Journal for Numer-

ical Methods in Fluids, 17:1055–1077, 1993.
8. J. Glimm, G. Marshall, and B. Plohr , *A generalized Riemann problem for quasi one-dimensional gas flows*, Adv. Appl. Math., 5:1–30, 1984.
9. E. Godlewski and P.-A. Raviart, *Hyperbolic Systems of Conservation Laws*, Ellipses, 1991.
10. E. Godlewski and P.-A. Raviart, *Numerical Approximation of Hyperbolic Systems of Conservation Laws*, Springer, New York, 1996.
11. S. K. Godunov, *A difference scheme for the numerical computation of discontinuous solutions of the equations of fluid dynamics*, Mat. Sbornik, 47:271–306, 1959.
12. J. Guckenheimer, *Shocks and rarefactions in two space dimensions*, Arch. Rational Mech. Anal., 59:281–291, 1975.
13. L. Hörmander, *Lectures on Nonlinear Hyperbolic Differential Equations*, Springer, New York, 1997.
14. O. Igra, J. Falcovitz, T. Meguro, K. Takayama, and W. Heilig, *Experimental and theoretical studies of shock wave propagation through double-bend ducts*, Journal of Fluid Mechanics, 437:255–282, 2001.
15. O. Igra, J. Falcovitz, H. Reichenbach, and W. Heilig, *Experimental and numerical study of the interaction between a planar shock wave and a square cavity*, Journal of Fluid Mechanics, 313:105–130, 1996.
16. O. Igra, L. Wang, and J. Falcovitz, *Non-stationary compressible flow in ducts with varying cross-section*, Proc. Instn. Mech. Engrs., Part G, 212:225–243, 1998.
17. O. Igra, L. Wang, J. Falcovitz, and W. Heilig, *Shock wave propagation in a branched duct*, Shock Waves, 8:375–381, 1998.
18. S. Kruzkov, *First order quasilinear equations with several space variables*, Mat. Sbornik, English Transl. Math USSR-Sbornik, 10:217–243, 1970.
19. C. D. Landau and E. M. Lifshitz, *Fluid Mechanics*, Pergamon Press, New York, second edition, 1987.
20. J. Li, S. Yang, and T. Zhang, *The Two-Dimensional Riemann Problem in Gasdynamics*, Pitman, first edition, 1998.
21. H. W. Liepmann and A. Roshko, *Elements of Gasdynamics*, John Wiley, New York, first edition, 1957.
22. W. F. Noh, *CEL: A time dependent two-space-dimensional, coupled Eulerian-Lagrangian code*, In B. Alder, S. Fernbach, and M. Rotenberg, editors, *Methods in Computational Physics*, volume 3, pages 117–179. Academic Press, New York, 1964.
23. X. Rogue, G. Rodriguez, J. F. Haas, and R. Saurel, *Shock-induced fluidization of a dense bed of particles*, In A.F.P. Houwing, editor, *Proceedings of the* 21^{st} *International Symposium on Shock Waves*, Great Keppel Island, Australia, paper 2591, 1997.
24. A. H. Shapiro, *The Dynamics and Thermodynamics of Compressible Fluid Flow*, Ronald, New York, first edition, 1953.
25. J. Smoller, *Shock Waves and Reaction–Diffusion Equations*, Springer, New York, 1983.
26. G. Strang, *On the construction and comparison of difference schemes*,

SIAM Journal on Numerical Analysis, 5:506–517, 1968.
27. B. van Leer, *Towards the ultimate conservative difference scheme V*, Journal of Computational Physics, 32:101–136, 1979.
28. A. I. Vol'pert, *The space BV and quasilinear equations*, Mat. Sbornik, English Transl. Math USSR-Sbornik, 2:225–267, 1967.
29. D. H. Wagner, *The Riemann problem in two space dimensions for a single conservation law*, SIAM Journal on Mathematical Analysis, 14:534–559, 1983.
30. P. Zhang and T. Zhang, *Generalized characteristic analysis and Guckenheimer structure*, J. Differential Equations, 152:409–430, 1999.
31. B. Zingerman, R. Alimi, S. Wald, and J. Falcovitz, *Lagrange-Euler scheme for heterogeneous gas-grain flow*, In R. Hillier, editor, *Proceedings of the* 22^{nd} *International Symposium on Shock Waves*, Imperial College, London, UK, pages 1423–1428. University of Southampton, Southampton, 1999.